

Review

Cracking and Toughening Mechanisms in Nanoscale Metallic Multilayer Films: A Brief Review

Qing Zhou * , Yue Ren, Yin Du, Dongpeng Hua and Weichao Han

State Key Laboratory of Solidification Processing, Center of Advanced Lubrication and Seal Materials, Northwestern Polytechnical University, Xi'an 710072, Shaanxi, China; renyue@nwpu.edu.cn (Y.R.); duyin@nwpu.edu.cn (Y.D.); huadongpeng@nwpu.edu.cn (D.H.); hanweichao@nwpu.edu.cn (W.H.)

* Correspondence: zhouqing@nwpu.edu.cn

Received: 5 September 2018; Accepted: 25 September 2018; Published: 4 October 2018



Abstract: Nanoscale metallic multilayer films (NMMFs) have captured scientific interests on their mechanical responses. Compared with the properties of monolithic films, multilayers possess unique high strength as the individual layer thickness reduces to the nanoscale, which is benefited from the plentiful hetero-interfaces. However, NMMFs always exhibit a low fracture toughness and ductility, which seriously hinders their practical applications. While there have been reviews on the strengthening and deformation mechanisms of microlaminate, rapid developments in nanotechnology have brought an urgent requirement for an overview focused on the cracking and toughening mechanisms in nanoscale metallic multilayers. This article provides an extensive review on the structure, standard methodology and fracture mechanisms of NMMFs. A number of issues about the crack-related properties of NMMFs have been displayed, such as fracture toughness, wear resistance, adhesion energy, and plastic instability. Taken together, it is hoped that this review will achieve the following two purposes: (1) introducing the size-dependent cracking and toughness performance in NMMFs; and (2) offer a better understanding of the role interfaces displayed in toughening mechanisms. Finally, we list a few questions we concerned, which may shed light on further development.

Keywords: nanoscale metallic multilayer; cracking; fracture behavior; toughening

1. Introduction

Composite materials with unique mechanical properties were widely applied long before the discipline of materials science existed. Depositing multiple materials in turns can produce the multilayered structure, among which metal/metal and metal/ceramic multilayers are well studied [1,2]. Particularly, owing to their unusual mechanical, electrical and magnetic properties provided by different metallic phases, nanoscale metallic multilayer films (NMMFs) are promising for micro-electro-mechanical systems. Additionally, the tunable length scale and interface features enable NMMF a basic model for the fundamental studies of length-scale and interface-structure dependent mechanical properties in metal and alloys. Generally, the strength of NMMFs often exhibit an order-of-magnitude increase [1–4] without overly compromising ductility [5–8]. Generally, the strength of NMMFs can approach 1/3 of the theoretical strength $\mu/30$ of GPa-level [3]. The strengthening effect is always related to the structure nature of the bicrystal interfaces [9–11].

Therefore, the essential concept of mechanical behavior in NMMFs is that, unlike bulk composites following the rule-of-mixtures law, the volume fraction of the constituent phase is not the pivotal factor. In particular, as numerous studies concerning the strengthening effects, recent studies have focused on the role of interface in material toughening [5,8,10,12–16]. Similar to the strengthening effect identified in NMMFs, both the layer thickness and the specific interface structures become the decisive parameters

to control fracture behavior and toughening process in NMMFs. Then the interface engineering, which is considered as achieving the desired properties by effectively controlling the distribution of heterophase interface and interfacial character, has been a main job in material science and engineering. However, pioneer understanding stays in a phenomenal level that interfaces act as obstacles to cracks. From this aspect, the well-defined layer structure and continuous interface in NMMFs provide essentially conditions for accurate understanding the crack-interface interaction. Thus, the remainder of this paper focuses on selected efforts in the field, classified by microstructure, mechanical as well as fracture-related properties in NMMFs, aiming to uncover the underlying plasticity deformation and toughening mechanism, which is considered essential for designing multilayers.

2. Microstructure

2.1. Interface Structure

NMMFs with high interfacial density and controllable length scale are always fabricated via physical vapor deposition (PVD) and electro-deposition (ED). Starting from a substrate (rigid Si or compliant polymer), two different metals deposit on each other alternately, until the expected layer thickness is attained. Between two phases, an atomically sharp interface can be formed, which has been classified into three groups: coherent interface, semi-coherent interface and incoherent interface.

Layers of materials between coherent interfaces are with identical crystallographic structure and approximate lattice parameter, commonly appeared in fcc/fcc multilayers, such as Cu/Ni [17]. The slip systems are nearly continuous across the adjacent layers; dislocations can pass across the coherent interfaces (Figure 1). But the small lattice mismatch of the interface can result in high coherent stresses, leading to the enhanced hardness/strength of multilayers.

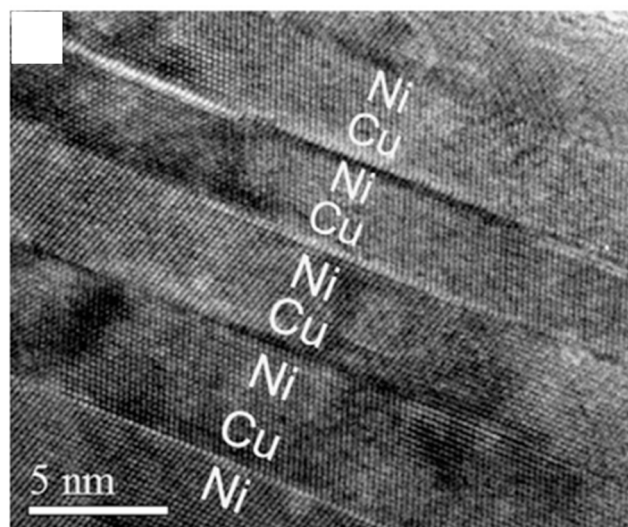


Figure 1. HRTEM image of full coherent interfaces [17].

The same as coherent interfaces, there is the same crystallographic structure in two layers with semi-coherent interfaces, but with larger lattice mismatch. Semi-coherent interfaces are commonly appeared in multilayer systems which have large lattice mismatch. Misfit dislocation is often introduced to relieve the severe lattice distortion. Consequently, the dislocations at the interface attributes to the interface barrier. On the other hand, semi-coherent interface are likely to transform to coherent interface as h is small enough (smaller than the critical thickness h_c). Information about interface structure evolution with the variation of h are shown later in Section 2.2.2.

The interfaces with distinct lattice structures, which possess a high lattice mismatch, are incoherent interfaces. Incoherent interfaces are commonly appeared in fcc/bcc multilayers [18,19]. TEM photos

(Figure 2a) and molecular simulations (Figure 2b) have shown that the interfaces possess a well-defined pattern of misfits (Figure 2c,d).

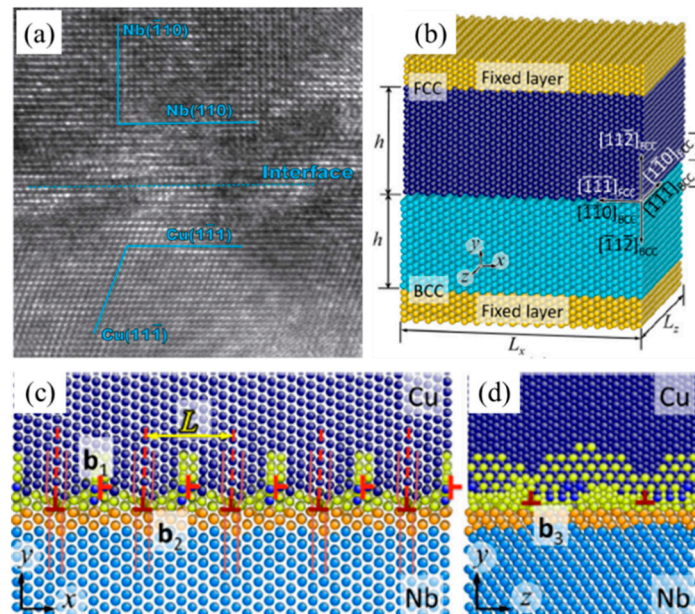


Figure 2. (a) HRTEM micrographs of the Cu/Nb interface in a PVD nanolayered composite; (b) Molecular simulation model of a Cu/Nb bi-layer. (c,d) are intrinsic defect structures (misfit dislocations) at the Cu/Nb interface [18].

2.2. Dimensionally-Induced Structural Transformations

2.2.1. Phase Structure Transformation

Phase structure transformation, which is difficult for the bulks, can be directly detected in NMMFs since a great deal of interfaces can be the nucleation sites for phase transformation. Transformation of lattice structures often occurred when h is small [20,21]. HRTEM images of (111) Cu/Co multilayers in Figure 3a shows that an fcc Co layer first formed on Cu, followed by an hcp Co layer. The orientation relationship between fcc and hcp Co is shown in Figure 3b. For Al/Ti multilayers [22], the interesting sequence of crystal structure transformation has also been reported.

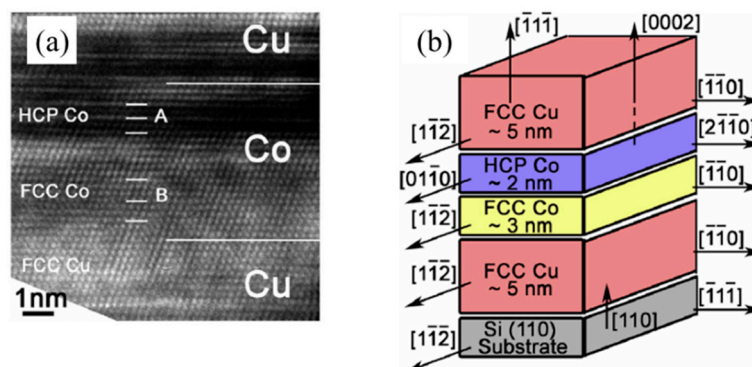


Figure 3. (a) HRTEM image of Cu/Co NMMFs with $h = 5$ nm reveals the coexistence of hcp and fcc Co. (b) The corresponding orientation relationship [20].

To account for polymorphic stability, three theories are proposed to understand the phase transformation in NMMFs, involving the influences of stacking fault energies [23] and coherency strains [24]. A thermodynamic approach [22,25] considering the large excess energy associated with

thermally preferred interfaces is often believed to account for the phase transformation. The total energy of the bilayer was proposed to be at the minimum energy configuration. Following Banerjee [22], the specific free energy Δg could be described by Equation (1) for formation of a A/B bilayer:

$$\Delta g = 2\Delta\gamma + [\Delta G_{Al}f_{Al} + \Delta G_{Ti}f_{Ti}]\lambda \tag{1}$$

where $\Delta\gamma$ is the change in interfacial free energy, Δg figuratively denotes the free energy change of the constituent [22]. λ is bilayer thickness. As λ reduced from its maximum value, Δg should be 0 if both metals have their stable crystal structures as represented by the horizontal line shown in Figure 4. Driven by $\Delta g < 0$, the transformation of Ti from hcp to fcc structure is attributed to the slope of the line fcc/fcc is smaller than that of the line hcp/fcc when $\lambda < \lambda^*_{fcc/fcc}$. As λ further reduced to or below $\lambda^*_{hcp/hcp}$, the energy of the system can be reduced by transforming Al from fcc to hcp structure, resulting Al-hcp/Ti-hcp multilayers.

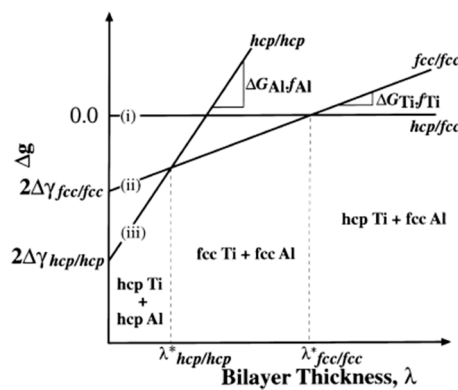


Figure 4. Stability diagram plotting Δg as a function of λ [22].

Considering fcc and hcp are adapting the same closed packed structure, phase transformation appeared more easily. While this phenomenon can also been observed in bcc metal [21,26]. For example, a metastable bcc Mg was reported [21] in Mg/Nb multilayers (Figure 5a); phase stability diagrams of Co/Cr, Zr/Nb and Ti/Nb multilayers are provided also [26]. When a transition occurs from fcc to bcc, the corresponding difference of the interfacial energies $\Delta\gamma$ is as follows:

$$\Delta\gamma = \gamma_{in} - \gamma_c = \frac{4\bar{a}\bar{S}_{vib}\bar{H}_m}{3\bar{V}_m R} - \frac{\mu_A\mu_B\bar{a}a_B}{2\pi(\mu_A + \mu_B)|a_B - a_A|(1 + \nu)} \times \left(\ln\left(\frac{a_B}{2|a_B - a_A|}\right) + 1\right) \tag{2}$$

where γ_{in} and γ_c are the incoherent and coherent interface energy for fcc/bcc and fcc/fcc respectively; μ and a are the shear modulus and atomic radiuses; R is the ideal gas constant, ν is the Poisson ratio; \bar{a} , \bar{H}_m , \bar{S}_{vib} , and \bar{V}_m are the mean values of the atomic diameter, the melting enthalpy, the vibration part of the overall melting entropy and the molar volumes of corresponding substances consisting of interfaces, respectively. According to Equations (1) and (2), the bi-phase diagram representing phase stability as a function of reciprocal scale ($1/\lambda$) and composition (in this case f_{Nb}) is used to construct the structure transformation in the NMMFs as shown in Figure 5b. Then the microstructure of NMMFs can be effectively controlled by tailoring their layer thickness and composition.

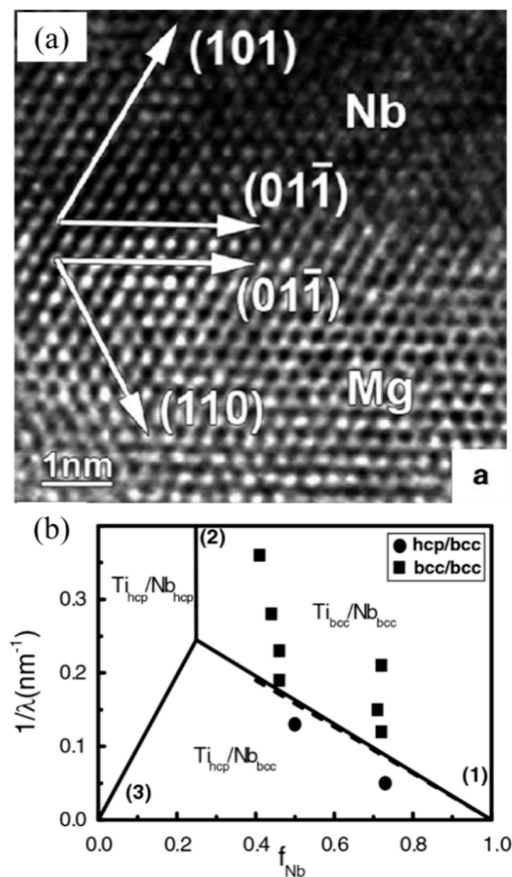


Figure 5. (a) HRTEM of the Mg/Nb multilayer shows the metastable bcc Mg; (b) The structure transformation diagram of Ti/Nb multilayers [21,26].

However, with regard to fcc/bcc NMMFs phase structure transition must be achieved under more rigorous conditions [27–29]. The common way to shrink characteristic dimensions toward to nanoregime also works in Cu/Fe NMMFs. However, fcc Fe can only be observed when h is as small as 0.75 nm [30]. Large shear stress induced by misfit strain energy in fcc/bcc NMMFs commonly plays an important role. The phase transition of Nb has been found in Cu/Nb NMMFs [27]. Additionally, a continuous and reversible bcc–fcc phase transformation via a rotation of bcc {110} or fcc {111} planes is observed in the Bain orientation in V/Ag NMMFs [29]. The large stress for structure transition to operate is also dependent on the length scale. Molecular dynamics simulations reveal that the deposited Cu layer initially grows as bcc with misfit located at interface [31]. The phase transition is also detected in Al/W NMMFs with a fixed 5 nm W layer experimentally [28], bcc Al layers was observed in 1 nm Al and 5 nm W NMMF despite the large lattice mismatch and significantly different lattice structures between Al and W. However, bcc Al does not appear in Al/W with equal individual layer thickness of 5 nm because of the reduction of high interfacial stresses.

2.2.2. Interface Structure Evolution

The degree of epitaxy, coherency, and texture of multilayers increased with decreasing h in fcc/fcc, hcp/hcp, and fcc/hcp NMMFs. For fcc/fcc Ag/Al [4] with lattice parameter mismatch is <1%, only a single peak was present in XRD results as shown in Figure 6a, indicating epitaxial character for all multilayers; for hcp/hcp Mg/Ti [32], epitaxial deposition between Mg and Ti matching the basal plane has been the prevalent growth mode as h is small enough, in spite of the relatively large lattice mismatch between Mg and Ti (Figure 6b); for fcc/hcp Cu/Co [20], interface structure evolution will experience different stages as h decreases (Figures 3 and 6c). The moderate lattice mismatch between Cu and Co indicated that the interface of the Cu/Co multilayers should be semi-coherent at best.

At the Cu/Co interface, dis-registry of atoms could be replaced by misfit dislocations periodically. The equilibrium spacing of misfit dislocations is given as:

$$s = b/\epsilon \tag{3}$$

$$h_c = \frac{b}{8\pi\epsilon(1 + \nu)} \left(\ln \frac{h_c}{b} + 1 \right) \tag{4}$$

In general, as suggested by Matthews and Hoagland [33–36], the critical thickness h_c for epitaxial growth could be larger than the calculated value by Equation (4) since other strain relaxation factors, such as the elastic isotropy, linear elastic strain in the lattices or difficulties associated with the formation of misfit dislocations, are involved.

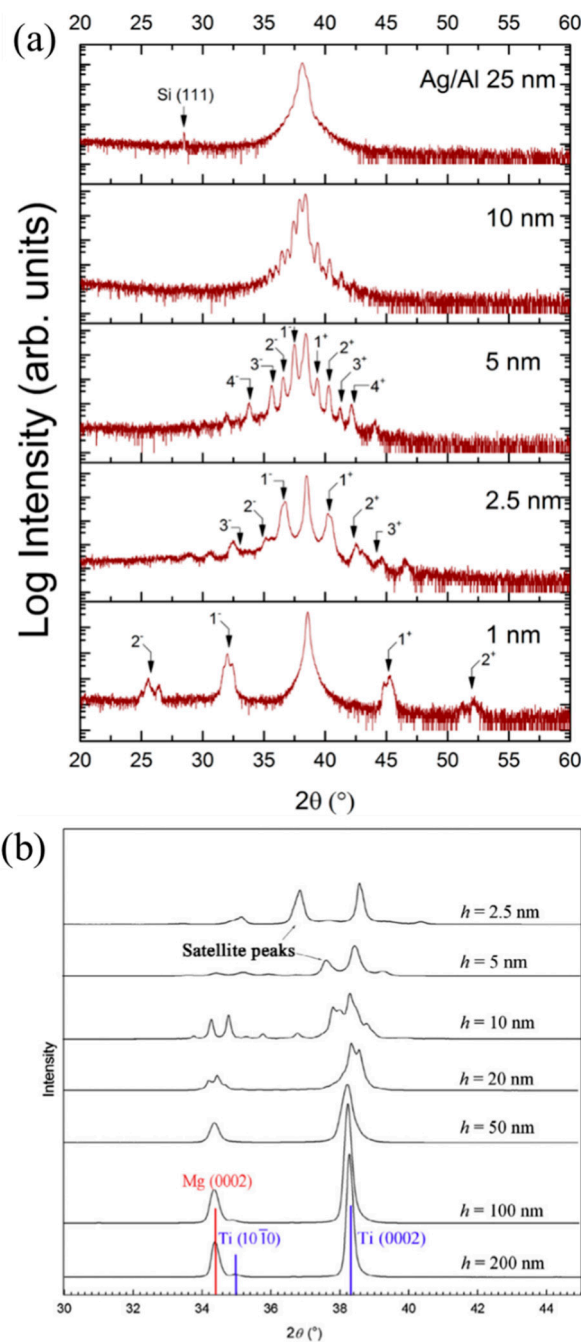


Figure 6. Cont.

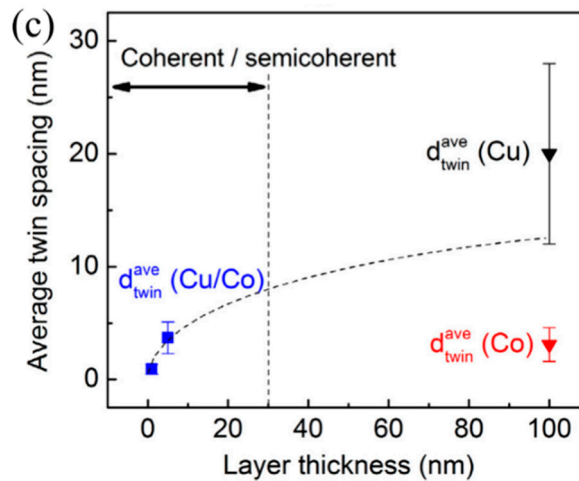


Figure 6. (a) XRD profiles of Ag/Al multilayer films with varying h , showing epitaxial character for all multilayer films. Only a single peak was present when h reduced to 25 nm. As h decreased to 10 nm, satellite peaks of multiple orders began to appear; (b) XRD results of Mg/Ti NMMFs with h ranges from 2.5 nm to 200 nm. The primary diffraction peaks correspond to Mg (0002) and Ti (0002) (the basal planes). For large individual layer thickness, Ti (10-10) reflections also become visible. It is observed that the peak breadth becomes larger with decreasing h . Satellite peaks start to emerge around the primary peaks at small h . (c) The interface structure evolution with layer thickness h in (111) Cu/Co multilayers. Note that the interface is coherent at $h < 25$ nm, while the interface is semicoherent at $h > 25$ nm [4,20,32].

3. Basic Mechanical Properties

3.1. Experiment Methods

The methodologies employed to measure mechanical and fracture properties for NMMFs fall into one of these methods: nanoindentation, uniaxial tensile, micropillar compression, bending, and scratching, which are discussed in detail below.

3.1.1. Nanoindentation

Nanoindentation is the most popular protocol in assessment of mechanical properties for NMMFs. A scanning electron micrograph of the nanoindentation residual impression of an Ag/Co NMMFs is shown in Figure 7a [37]. The hardness and elastic modulus are measured with nanoindentation [38,39]. In addition, this technique is also available for measuring strain rate sensitivity, the stress exponent for creep, activation energy and fracture behavior [15,40–43]. A typical set of load-displacement data are presented in Figure 7b, which also serves to define some experimental quantities. The key quantities are the peak load P_{max} , the maximum displacement h_{max} , and the projected contact area of the impression A . For nanoindentation, the contact stiffness with the contact area in conjunction provides a valid measurement of the hardness H and elastic modulus E_{eff} as:

$$H = P_{\text{max}} / A \tag{5}$$

and:

$$E_{\text{eff}} = \frac{1}{\beta} \frac{\sqrt{\pi}}{2} \frac{S}{\sqrt{A}} \tag{6}$$

where β is a constant which depends on the geometry of the indenter. The effective modulus, which is responsible for the fact that elastic deformation occurs in both the specimen and the indenter, is given by:

$$\frac{1}{E_{eff}} = \frac{1 - \nu^2}{E} + \frac{1 - \nu_i^2}{E_i} \tag{7}$$

where E and ν are the Young’s modulus and Poisson’s ratio for the specimen, and E_i and ν_i are the same quantities for the indenter [38].

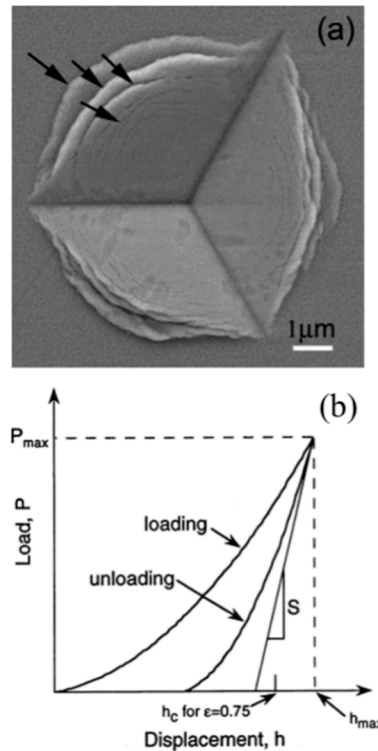


Figure 7. (a) SEM images of indents on Ag/Co multilayer. (b) Typical indentation load-displacement data defining key experimental quantities [37,44].

Equation (7) is suitable to a thin film on a substrate as long as the multilayer and substrate have the same elastic properties. If the multilayer and substrate are elastically inhomogeneous, a simple model developed by Doerner and Nix [45] is used in order to avoid the substrate effects on the intrinsic modulus of the NMMFs as:

$$\frac{1}{E} = \frac{1}{E_i} + \left(\frac{1}{E_s} - \frac{1}{E_m} \right) \exp\left(-\alpha \frac{h_f}{h_0}\right) \tag{8}$$

where α is a constant, h_f is the multilayer thickness and h_0 is the penetration depth.

3.1.2. Uniaxial Tensile

Since nanoindentation has been the primary mechanical test method, the nominal strain to failure data for NMMFs is limited, Uniaxial tensile testing can cover this shortage [8,12,46–48]. During tensile testing, the strain and stress were automatically recorded by machine and then Young’s modulus of the film/substrate system (E_{total}) and the substrate (E_s), and the yield strength of the film/substrate system (σ_{total}) and the substrate (σ_s) are calculated from the σ - ϵ curve [49–51]. The yield strength (σ_y) is determined as the 0.2% offset. Accordingly, Young’s modulus (E_f) and the yield strength (σ_f) of the NMMFs can be determined from the following equations [51]:

$$E_f = (t_{sb}/t_f)(E_{total} - E_s) \tag{9}$$

and:

$$\sigma_f = (t_{sb}/t_f)(\sigma_{total} - \sigma_s) \tag{10}$$

A macroscopic strain (ϵ_c) obtained from the R - ϵ curves [49] is used to characterize the ductility. Respective SEM images are often shown thereafter to characterize the fracture behavior, as shown in Cu/Nb NMMFs in Figure 8 [52]. The cracking of brittle films is described analytically with a 2-D steady-state models [53], in which the steady-state energy release rate ζ can be described as [53]:

$$\zeta = \frac{\pi\sigma^2 t}{2E}(1 - \nu^2)g(\alpha_1, \alpha_2) \quad (11)$$

where E is the Young's modulus of the NMMFs; σ is the tensile stress of NMMFs at ϵ_c ; t is the multilayer thickness; and $g(\alpha, \beta)$ is calculated from the elastic mismatch between the film and substrate, with α_1 and α_2 being the two Dundurs' parameters [54]. The fracture toughness (K_{IC}) of the NMMFs is generally expressed as [55]:

$$K_{IC} = \sqrt{\frac{E\zeta}{1 - \nu^2}} \quad (12)$$

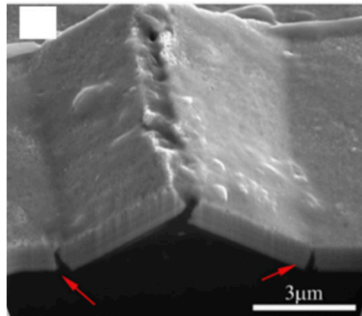


Figure 8. Respective SEM images showing the buckles in Cu/Nb NMMFs after uniaxial tensile testing [52].

3.1.3. Flat Punch Micropillar Compression

For NMMFs, when h is below 20 nm, tensile tests reveal that insignificant deformability occurs in the test specimens as a result of small flaws [56]. In this condition, stress-strain curves and the ductility are not available using traditional methods. However, micropillar compression testing which enables measurement of stress-strain response at small h has been successfully used to investigate the mechanical performance of NMMFs [5,13,57]. Focused ion beam machining has created opportunities for fabricating micropillar NMMFs, where a sample is shaped with a high precision using a Ga⁺ ion beam [58,59]. Figure 9 shows such a pillar with the layer direction perpendicular to the cylinder axis.

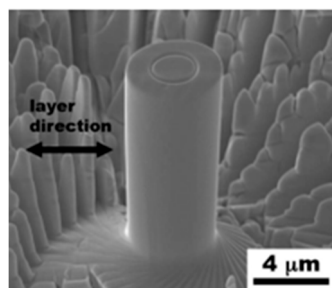


Figure 9. SEM micrograph of the micropillar of Cu/Nb multilayer with $h = 5$ nm. The layer interfaces are perpendicular to the cylinder axis [5].

The microcompression test was performed with a flat punch diamond indenter. During testing, force–displacement data were continuously recorded, and a constant volume is used to calculate the true stress–strain curves, the homogeneous deformation assumption model is applied to characterize

the deformation behavior [57,60]. Considering the substrate effect and taper influences, the true strain ε_T and true stress σ_T are expressed as [60]:

$$\varepsilon_T = \frac{1 + (L_0/r_0) \tan \psi}{E_{measured}} \frac{PL_p}{A_0L_0} + \ln\left(\frac{L_0}{L_p}\right) \tag{13}$$

and:

$$\sigma_T = \frac{P}{A_0L_0} \left\{ L_0 - \left[\mu_{tot} - \frac{PL_{Su}}{E_{Su}A_{Su}} - \frac{\sqrt{\pi}P(1 - \nu^2)}{2E_{Su}\sqrt{A_{Su}}} \right] \right\} \tag{14}$$

where A_0 is the cross-sectional area at half initial height (L_0) of the pillar; r_0 is the radius at the top of the pillar; L_p is the final height of the pillar; P is the load and $E_{measured}$ is the measured modulus of the tapered NMMFs determined from the unloading segments at strains between 1% and 5%; u_{tot} is the total displacement; A_{Su} , L_{Su} and E_{Su} are the average cross-sectional area, the total length and the modulus of the substrate pillar, respectively. The yield strength of micropillars is no longer expressed by flow stress at strain of 0.2%. Since large stress strain scatter is generally observed in the initial stage of plastic flow, the flow stress at a relatively large amount of strain (2%) is chosen [60,61].

In general, the macroscopic deformability of these NMMFs micropillars, as well as the deformation behavior (homogeneous vs. in-homogeneous), has been a hot topics in the current literatures. Additionally, most of the micropillar work pays close attention to the effects of sample size i.e., pillar diameter on the yield strength [62–64]. In contrast, in small-scaled materials such as NMMFs, the extrinsic size and intrinsic size overlap in general. Unlike traditional nanoindentation test leading to a non-uniform stress state in the plastic zone within the sample [65,66], the microcompression methodology opened a new avenue for studying the origin of deformation instability in NMMFs with a nominally homogeneous stress state [61].

3.1.4. Bending

Three-point bending tests are another testing method focusing on the fracture properties of NMMFs. Although tensile testing and micropillar compression are considered to be a direct and effective way determining the intrinsic plasticity/ductility properties, owing to difficulties with the experiments, three-point bending tests can be chosen to acquire the processes of deformation and fracture. Manufacturing a precrack, loading to induce crack propagation, measuring the critical stress needed to inflict fracture, and observing the fracture morphology is followed as a simple procedure to conduct. Figure 10 is the schematic illustration of three-point bending apparatus used for localized fracture experiment in NMMF [67]. It should be noted that the NMMF must be thin enough relative to the substrate in order to eliminate the effects of stress non-homogeneity at the crack tip. Figure 11 is a fractography of Cu/Au multilayer specimens [67]. During the bending processes, the energy difference (ΔU_e) would represent the energy required to enable cracking of the film if the substrate remained elastic. The critical energy release rate ζ_c can be described as [68]:

$$\zeta_c = -\frac{dU_e}{dA_c} = -\frac{\frac{1}{2}\Delta F^2 \cdot dC}{2h \cdot dr} \tag{15}$$

where U_e is the elastic energy, A_c is the area of the crack, h is the film thickness, dC/dr is the change in the compliance (C) of the film with respect to the change in crack length (r), ΔF is the measured force difference. For NMMFs, fracture toughness can be calculated through:

$$K_c = \sqrt{E\zeta_c} \tag{16}$$

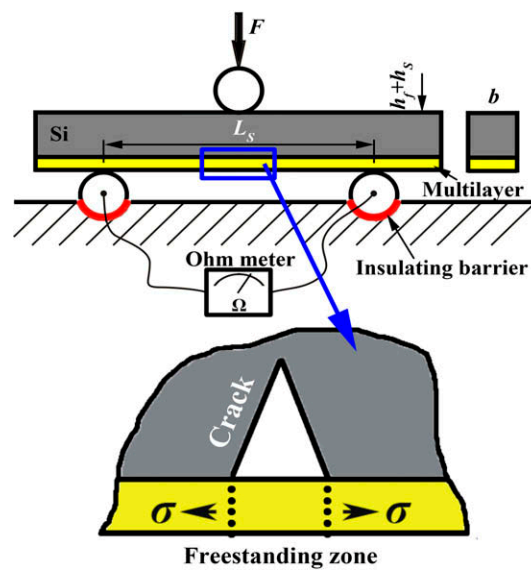


Figure 10. Schematic illustration of three-point bending apparatus used for localized fracture experiment [67].

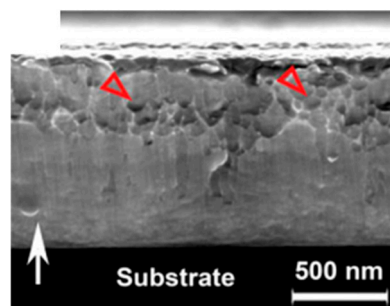


Figure 11. Fractography of Cu/Au multilayer specimens with $h = 25$ nm. The shearing direction is indicated by white arrows [67].

3.1.5. Scratching

Scratch test is generally considered as one of the simple means in assessing adhesion strength of a film on its substrate [69–71]. Additionally, it has been widely used to evaluate the bonding strength [72] and tribological behaviors (friction and wear) of thin films [73,74]. The nanoscratch technique provides a simple, versatile and rapid means to assess the scratch wear resistance among the techniques available to evaluate the nanotribological properties of thin films. Generally speaking, for brittle films, microcracks appear prior to the film adhesion failure [75]. The load corresponding to the crack initiation is often referred to cracking resistance. The coefficient of friction of NMMFs are found to increase with the scratch length, and the rate of increase has been found notably depending upon the periodicity of NMMFs [76].

3.2. Yield Strength/Hardness

Original attraction in metallic NMMFs comes from the order-of-magnitude increases in yield strength accompanied by the decrease of h [77]. Hardness of the NMMF is acquired by multiplying reported tensile yield strengths by 2.7 [56]. The attention is mainly focused on $h < 100$ nm with the rapid development of nanotechnology. NMMFs are suitable for fundamental studies on the effects of length scale, in the range of micrometers and nanometers thickness, on the deformation mechanisms in metallic nanocomposites. Misra et al. [78] produced Figure 12 to summarize the deformation regimes in metallic multilayer thin films as a function of individual layer thickness h . Under a constant modulation ratio of 1, the hardness/strength curve of NMMFs usually exhibits three different regions:

Hall–Petch, confined slip in single layer, and interface crossing. Among the numerous studies, extensive works have been experimentally and theoretically conducted on Cu–Ni [14,17,57,77,79–85] and Cu–Nb [1,5,6,27,42,78,81,86,87] systems. Tables 1 and 2 compares peak hardness (H_{max}), crystal structure and the hardness enhancement for the extensive investigated Cu/X and Ag/X NMMFs. The hardness enhancement is calculated from the hardness ratio of H_{max} with the rule-of-mixtures hardness (H_{rom}) of the monolithic constituent films.

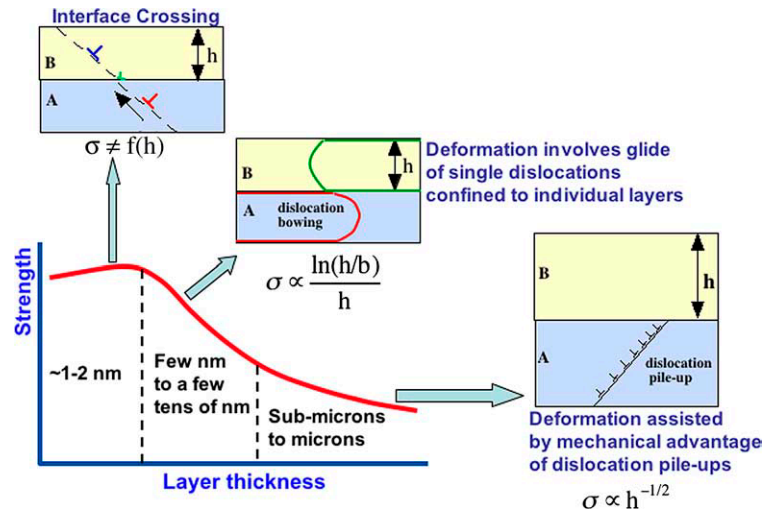


Figure 12. Deformation mechanisms active at different length scales [78].

Table 1. Peak hardness H_{max} and hardness enhancement H_{max}/H_{rom} for a variety of Cu/X multilayers.

Systems (Cu/X)	Layer Thickness, h nm	Peak Hardness, H_{max} GPa	H_{max}/H_{rom}	References
Cu/Ni	1.75	6.83	1.89	[17]
Cu/Au	25	2.45	1.23	[88]
Cu/Co	1	6	1.60	[20]
Cu/Nb	1.2	7.02	3.15	[78]
Cu/Fe	5	4.8	1.49	[30]
Cu/V	2.5	5.2	1.56	[89]
Cu/Cr	10	6.8	1.36	[1]
Cu/W	4	8.9	1.25	[90]
Cu/Ta	30	7.0	1.08	[91]
Cu/Zr	5	5.8	1.54	[92]
Cu/Ru	5	8.1	1.16	[48]

Table 2. Peak hardness H_{max} and hardness enhancement H_{max}/H_{rom} for a variety of Ag/X multilayers.

Systems (Ag/X)	Layer Thickness, h nm	Peak Hardness, H_{max} GPa	H_{max}/H_{rom}	References
Ag/Cu	2	4.6	1.70	[93]
Ag/Ni	5	6.2	1.48	[94]
Ag/Al	5	5.5	3.67	[4]
Ag/Co	3.5	4.9	1.23	[39]
Ag/Nb	2	7.9	2.26	[95]
Ag/V	4	5.7	1.63	[96]
Ag/Fe	2	6.36	1.51	[97]
Ag/W	50	3.36	0.25	[98]

3.3. Ductility

Figure 13 shows available maximum engineering strain at failure from micropillar compression [5,13,61,99–101] and tensile [87,102–105] tests. As expected, tensile tests have much smaller values, illustrating that tensile failure often involves crack nucleation. Generally, the ductility and strength of materials are exclusive with each other [106], i.e., the ductility of NMMFs decrease with decreasing h , showing an opposite trend to the strength [5,8,13,102]. For compression, failure often involves shear localization in the micropillar sample [13,107], as discussed later in Section 4.5.2. They compressed Cu/Nb NMMFs pillars and found that the ductility decreases from 36% to 25% as h is reduced from 40 nm to 5 nm by using nanoindentation testing [5,13]. Rolling strains of >60% without material failure is reported on nanoscale Cu/Nb multilayers [108,109]. However, Misra et al.'s [110] results showed that the rolling strain to fracture of Cu/Nb multilayers decreased rapidly as the h was less than about 30 nm.

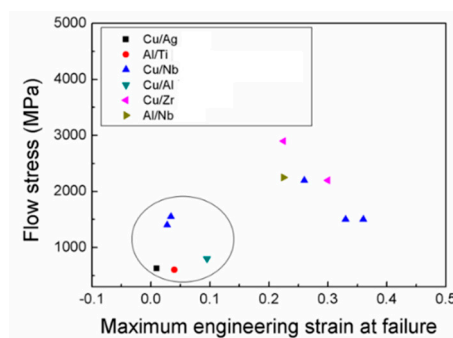


Figure 13. Flow stress versus maximum engineering strain at failure for various NMMFs with equal layer thickness. Circle indicates tensile data; remaining data are from micropillar compression tests. For all the cases, the individual layer thickness h is smaller than 100 nm.

4. Other Fracture Properties

4.1. Fracture Toughness

4.1.1. Length-Scale-Dependent of Fracture Behavior

The fracture mode of NMMFs was directly associated with the strengthening mechanism. Misra et al. [111] proposed a dislocation mechanism transition from Orowan bowing to interface crossing to interpret the limited ductility and fracture toughness. Zhu et al. [112] found that the Cu/Ta multilayer with thickness of 5 nm exhibited shear-mode fracture while the Cu/Ta multilayer with thickness of 125 nm fractured in an opening mode. According to the theoretical analyses, it is pronounced that the opening-mode and shear-mode fracture was relevant to interface crossing and Orowan bowing deformation mechanism, respectively. It further implies that the interface structure plays a key role in the fracture behavior of metallic multilayers, as discussed in Section 4.1.2.

Additionally, the deformation and fracture behavior also display a strong length scale effect. When decreasing h , both the ductility and fracture toughness of NMMFs increase until a critical h_{cri} . Below h_{cri} the ductility and fracture toughness decrease with reducing h [8,48,52]. The size-dependent toughness shown here indicates that the failure mechanisms for NMMFs are complex and the controlling mechanisms are completely different in the two regions above and below h_{cri} .

The fracture behavior in A/B NMMFs, which consists of alternating ductile (A) and brittle (B) layers, can be characterized by a micromechanical model [8,55,113]. The deformation capability of the ductile layers can be quantitatively obtained by an equilibrium number of dislocations accumulated in the A layer. Once the crack nucleated in the brittle B layer, it will propagate easily throughout the entire B layer and arrested by the interface, accompanied with high stress concentration around the crack tips. Crack propagation is caused by the variation in applied stress intensity, crack-tip

shielding induced by the plastic deformation, and the capacity to accommodate the activity of crack-tip dislocation [8]. Dislocations may emit from the microcrack tip with two effects: firstly, the crack tip is blunted by the emitted dislocations and the stress concentration around crack tip is reduced (Figure 14a). Consequently, it is difficult to achieve the cohesive strength of A layers and the fracture progress is improved; Secondly, once dislocations hindered by the interface (Figure 14a), they send a stress back to the crack tip. Further dislocation emission will be impeded by the back stress and fracture progress is reduced. The equilibrium number of dislocations at a specific load is [8,113]:

$$n = \frac{4\pi(1 - \nu)}{\ln(\tilde{h}/\tilde{r})} \left(\frac{\tilde{K}_{app} \sqrt{\tilde{h}}}{A\sqrt{2\pi}} \sin \phi \cos \frac{\phi}{2} - \tilde{\gamma} \right) \tag{17}$$

where $\phi = 45^\circ$ is the angle of inclination of the slip plane to the interface, $A \approx 1, \tilde{r} = 2.7r_0/b$, with r_0 being the effective core radius in A, the far field mode I stress intensity $K_{app} = 1.12\sigma_{app}\sqrt{\pi h}$ [55], $h_\phi = h/\sin \phi$, and the surface energy γ , respectively:

$$\tilde{K} = \frac{K_{app}}{\mu\sqrt{b}}, \tilde{h} = \frac{h_\phi}{b}, \tilde{\gamma} = \frac{\gamma}{\mu b} \tag{18}$$

The stress at the blunted crack tip $\tilde{\sigma}_{tip}$ is related to n and K_{app} :

$$\tilde{\sigma}_{tip}\sqrt{n} = 2\sqrt{\frac{2}{\pi}}\tilde{K}_{app}\left(1 - \frac{3(\sin \phi \cos \frac{\phi}{2})^2}{\ln(\tilde{h}/\tilde{r})}\right) + \frac{12A}{\sqrt{h}\ln(\tilde{h}/\tilde{r})}\tilde{\gamma}\sin \phi \cos \frac{\phi}{2} \tag{19}$$

The microcrack will propagate from a channel crack when the microcrack tip stress reaches the σ_c of the materials ($\tilde{\sigma}_{tip} = \tilde{\sigma}_c$). The maximum number (n_{max}) of equilibrium dislocations, which is generated from the crack tip before the cleavage in A layer can be obtained from Equations (17) and (19). Under this condition, the far-field applied stress intensity is then the fracture toughness of the multilayers, which could be obtained as $\tilde{K}_{IC} = \tilde{K}_{app}$.

The predicted n_{max} in Cu/Nb (see Figure 14b) apparently shows a size effect [8]. n_{max} increases sharply when h increases from 5 nm to 25 nm, Larger n_{max} means a better plastic deformation capability of Cu layers. The Cu layers is more ductile and hinder the crack propagation which comes from the brittle Nb layers. Additionally, with h increasing, the far field mode I stress intensity ahead of microcrack depends on the propagation of microcracks in Nb layer mainly, which is scaling with $h^{0.5}$ [114]. As a result, with increasing h , K increases, then the ductility and K_{IC} of NMMFs decrease. Meanwhile, a large ISF means that the microcrack is easily to propagate to form an opening fracture, the transition in fracture mode, which will occur from opening to shear at h_{cri} , is verified in Figure 15 [8]. In conclusion, the dominant factor which controls the modulation period and modulation ratio dependent fracture mode in NMMFs is the constraint effect from ductile layer on brittle layer [46].

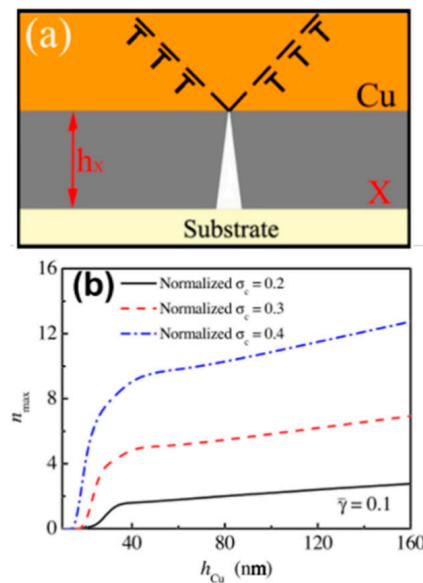


Figure 14. (a) Sketch of the micromechanical fracture model in NMMFs; (b) Model predicted n_{max} at different normalized cohesive strengths (σ_c) as a function of h [8].

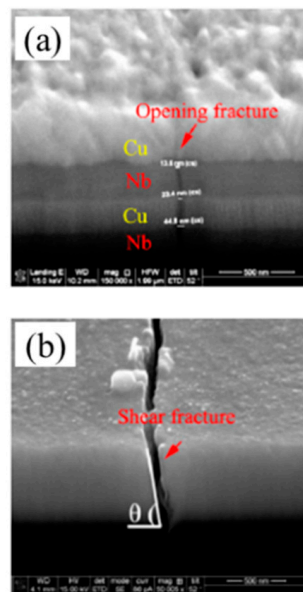


Figure 15. FIB cross-sectional images of microcracks of Cu/Nb NMMFs with (a) $h_{Cu} = 125$ nm and (b) $h_{Cu} = 5$ nm [8].

4.1.2. Phase Transformation Enhanced Toughening

A contradictory to the length scale dependent deformation and fracture mode in Cu/Nb NMMFs have been experimental observed in Cu/Ru multilayers, which indicated that the deformation mode changed from brittle cracking to ductile shearing with decreasing h [15]. With a relatively strong interface and small lattice mismatch in fcc/hcp Cu/Ru, the degree of coherency, texture, and epitaxy of multilayers increase with decreasing h , then the transmissibility for dislocation is much higher as the slip system between the layers was continuous across the interface. Then continuous dislocation emission process controls the crack blunting and growth processes (see in Figure 16). As the dislocations will not be constrained by the interface, the propagation of dislocations emitted from a crack can loosely move both in-plane and out-of-plane. In this condition, when the crack tip reaches interface with crack length equals to the thickness of Ru layers, the fracture toughness is obtained as [15]:

$$K_{IC} = mh^{-1/2} \quad (20)$$

where m is a constant of the NMMFs dependent on material systems. Equation (20) suggested that a small h is in favor of suppressing microcrack growth and increasing the fracture toughness. Furthermore, when h is decreasing, the slip continuity across interface increases, which provides more chances for dislocation transmission, thereby encouraging homogeneous deformation. Additionally, the strong bonding interface is more resistant to atomic decohesion compared to incoherent interface and, therefore, can store a larger amount of deformation-induced incompatibility before fracture occurs.

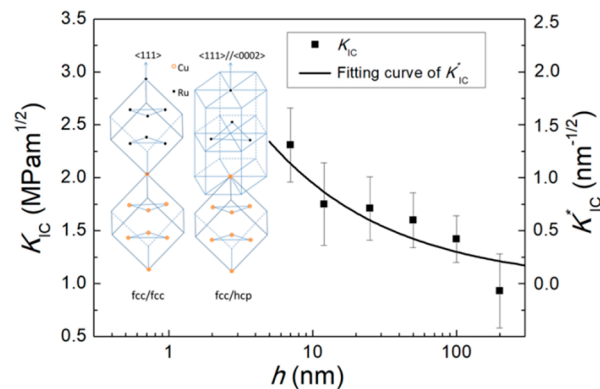


Figure 16. Dependence of K_{IC} on h (dots and left y-axis) for the Cu/Ru multilayers. Calculated normalized K_{IC} (lines and right y-axis) based on Equation (20) fits well with experimental results. Sketch shows the lattice structures transformation from the fcc/hcp to fcc/fcc epitaxial relationship, which determines the fracture toughness at small length scale [15].

On the other hand, the length scale dependent the fracture toughness of fcc/hcp NMMFS is also influenced by the transformation of lattice structures [15]. Due to the dimension induced phase transformation in Ru layer, the fcc/fcc Cu/Ru should possess a great deal of slip systems to accommodate plastic deformation; while, hcp Ru are difficult to deform due to few slip systems are available [21,115,116]. Accordingly, the difference in fracture toughness between fcc/hcp multilayers whether has structure transformation are summarized, as shown in Figure 17. Clearly, both the multilayers exhibit fracture toughness improvement with decreasing h first, which is account for the effective interface shielding effect on crack propagation. In contrast, at a relatively large h the fcc/bcc without structure transformation display a decrease trend in fracture toughness compared with the fcc/hcp multilayers with structure transformation. This decrease can be reasonably explained on the basis of the slip discontinuity of dislocations crossing the layer interface and thus broke down the interface shielding effect. While with further reducing h in fcc/hcp multilayers, the coherent trend accompanied with structure transformation makes the dislocations crossing interface process possible and elevate the fracture toughness. The complex cracking behaviors in a series of multilayers are functions of length scales and interface structures. This approach is potentially able to effectively explain ‘preparation–structure–properties’ relationships that are pointing to promising route for the optimized combination of toughness and strength. The experimental results and theoretical analyses are helpful to control the dimension configurations or constituent phases to achieve target toughening properties in NMMFs.

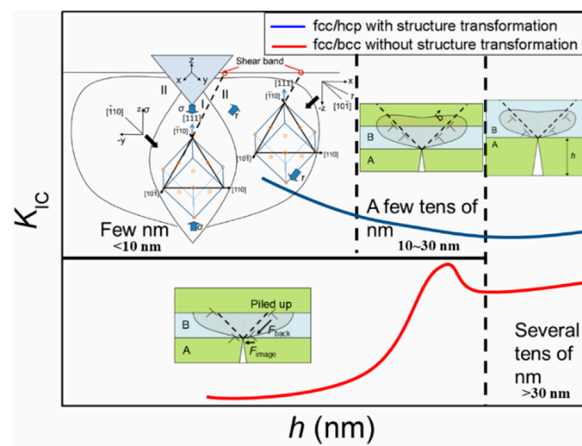


Figure 17. Evolution of fracture toughness with h for fcc/hcp multilayers with structure transformation and fcc/bcc without structure transformation. The figure demarcates regimes that exhibit distinct processes governing the crack and fracture phenomenon in this two multilayer systems. The sketches of the micro-mechanical fracture model, which shows the interface shielding effect, is presented in each region for clarity [15].

4.2. Wear Resistance

A great deal of excellent properties in metallic nanolayered composites has extensively aroused a great effort to explore the properties under more realistic operating environments, such as friction and wear. Films are often produced with NMMF materials owing large hardness, coating technology has motivated an extensive interest in application of wear resistance. Since significant hardness enhancement and a drastic softening are often observed in elastic modulus [9], a high ratio of H/E in multilayers which implies that they can induce the formation of self-organized microstructures with the potential improving wear resistance, as the ratio of hardness to elastic modulus has been proven as one of the significant parameters dominating a good wear resistance in a disparate range of materials [117].

Wen et al. [76] has systematically investigated the wear properties of Ag/Ni NMMFs. In multilayer with $h = 25$ nm, there are fluctuations in the friction coefficient after a scratch length of 250 μ m, which indicates the development of fine wear debris and possibly fracture. However, for multilayer with $h = 2.5$ nm, negligible fluctuation can be found at a scratch length about 350 μ m, indicating better wear behavior in multilayers with decreasing h .

4.3. Adhesion Energy

The performance of thin films all depend on adhesion between the substrate and the film [118–121]. Estimation of interfacial adhesion is also critically important in NMMFs [52,122]. In measuring NMMF adhesion, uniaxial tensile and indentation tests are generally preferred to initiate and drive delamination between film and substrate. The specific value of the interfacial adhesion energy Γ is related to the cracking and buckling processes as [52]:

$$\sqrt{\frac{\delta^*}{2h}} = (2\alpha)^{1/4} \frac{1}{2h} \left[1 + \sqrt{1 + \frac{3}{4}\alpha \left(\frac{l}{2h}\right)^4} \right]^{-1/4} \quad (21)$$

$$\alpha = 2\Gamma \left(\frac{2}{\pi}\right)^4 = \frac{4\Gamma_{cri}(1 - \nu_f^2)}{2hE_f} \left(\frac{2}{\pi}\right)^4 \quad (22)$$

where δ^* is the buckle height, l is the half of the buckle width, α is an experimentally calibrated parameter and h is the layer thickness. For nanoindentation, the strain energy release rate for a circular buckle due to residual and indentation stresses was calculated as [122]:

$$G = \frac{(1-\nu)H\sigma_r^2}{E}c\left[\left(1 - \frac{\sigma_c^2}{\sigma_r^2}\right) + \left(\frac{\sigma_v^2}{\sigma_r^2}\right)\left(\frac{2\sigma_c}{\sigma_v} + \frac{1+\nu}{2c} - 1\right)\right] \quad (23)$$

where:

$$\sigma_v = \frac{\beta EV}{a^2 h_f}, \sigma_c = \gamma E (h^*/a)^2, \beta = \frac{1}{2\pi(1-\nu)}, \gamma = \frac{k}{12(1-\nu^2)} \quad (24)$$

here, $c = [1 + 0.902(1-\nu)]^{-1}$ [123], a^* is the crack radius, h_f is the film thickness, V is the plastic volume displaced by the indenter, σ_r is the residual stress in the film, E and ν is the weighted elastic modulus and Poisson's ratio respectively.

Attention should be paid that the adhesion energy of NMMFs is related to the length scale when the modulation period λ is larger than 50 nm, as seen in Figure 18. Because the curvature of buckles inevitably causes a local deformation gradient, geometrically dislocations are required to accommodate the deformation discrepancy. At $\lambda < 50$ nm, dislocations slide individually in-plane within the constrained layers based on the discussion in Section 3.2. The buckles have smaller dimensions and mainly produce elastic deformation. As a result, the determined adhesion energy exhibits λ -independence (I regime in Figure 18) and is close to the intrinsic value. At $\lambda > 50$ nm, dislocations can move loosely both in-plane and out-of-plane within the layers. Buckles with greater dimensions can be formed since a larger deformation gradient can be accommodated, which leads to an overestimate of the adhesion energy due to the plastic deformation. The thicker λ the greater the plastic deformation, and vice versa. Therefore, a remarkable λ -dependence of adhesion energy is measured, shown as regime II in Figure 18.

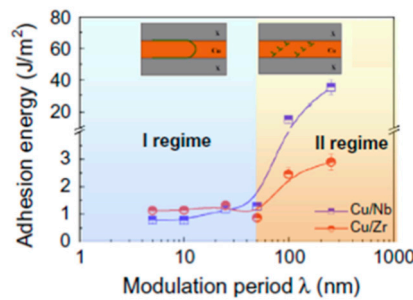


Figure 18. Length scale dependent deformation behavior on the evaluated adhesion energy in NMMFs. Two regimes divided by λ_{crit} represent the λ -independent and λ -dependent ranges, respectively [52].

4.4. Radiation Induced Embrittlement

With nuclear accidents occurring frequently in recent years, the safety and reliability of nuclear reactor operation gathered much attention in the materials community [124]. Helium (He) implanted in nuclear reactor components, both fuels and structural elements, causes changes in their chemical compositions and degrades their mechanical and thermal properties [125–127]. Thus, the urgent mechanical requirements for structure materials under irradiation environment are needed such as: thermal creep resistance, increased strength, neutron radiation damage resistance [124] and superior corrosion. The mechanical performance of structure materials is still a key factor restricting the service life of the reactor, operation stability and exchange efficiency in the advanced nuclear fusion/fission reactors. To extend the operating limits and lifetimes of nuclear reactors, the ability to prevent degrading material properties by the growth of bubbles and the subsequent formation of blisters is required [128,129].

Electron and light ion irradiation of crystalline solids leads to the creation of large numbers of vacancies and interstitials that agglomerate to form nanometer-sized bubbles, dislocation loops, stacking-fault tetrahedra and voids [128,130]. After irradiation, the defects (stacking-fault tetrahedra, cavities or dislocation loops) increase the stress requirement for yield and subsequent plastic flow, leading to irradiation hardening [96]. In conventional metals, radiation hardening is caused by the

interaction of dislocations with two types of radiation induced defects: strong obstacles such as stacking-fault tetrahedra, interstitial loops and interstitials, and relatively weak obstacles such as He bubbles [131]. A barrier model is developed to estimate strengthening mechanism due to strong barriers. The increase in yield strength $\Delta\sigma$ after radiation is expressed by:

$$\Delta\sigma = M\alpha'\mu b\sqrt{N_d d_i} \tag{25}$$

where M is the Taylor factor, α' is a parameter that depends on the average barrier strength, N_d is the defects density across the radiation damage region and d_i is the diameter of interstitial loops.

He bubble is treated as a weak obstacle when the bubble size is small enough. The FKH model is applied to estimate the He bubbles induced enhancement of yield strength, $\Delta\sigma$, by [132]:

$$\Delta\sigma = \frac{1}{8}M\mu b d_b N_d^{2/3} \tag{26}$$

Orowan model [133–135] produces another describing of the hardening effect due to the dislocation pinning at point obstacles. For strong obstacles with spacing l , it is assumed that the glide dislocation bows to a semicircle with a radius of $l/2$. However, weak obstacles are overcome at the applied shear stresses less than which is needed to bend the dislocation to a semicircle, thus the Friedel equation is adopted [133,134]:

$$\tau = \frac{\mu b}{2\pi L} \ln\left(\frac{L}{r_d \sqrt{\cos \varphi_c}}\right) (\cos \varphi_c)^{3/2} \tag{27}$$

$$L = \frac{1}{\sqrt{2N_d r_d}} \tag{28}$$

where r_d is the radius of the defect cluster and φ_c is half of a critical bow-out angle between lines of a dislocation cutting an obstacle (Figure 19).

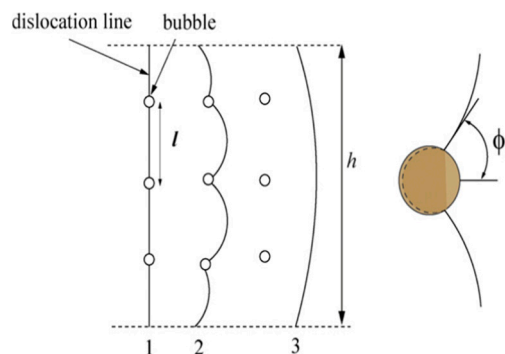


Figure 19. Schematic illustration of glide dislocation interactions with nanometer-scale bubbles with the spacing of l . Numbers 1–3 show the steps of dislocation movement across the bubbles. φ_c is the semi-critical angle at which the dislocation breaks away from the pinning points [96].

The radiation-induced hardening in NMMFs was found to decrease with decreasing individual layer thickness. No changes in hardness was measured in multilayers with h less than 10 nm in Ag/V after implantation [96]. In the case of CLS, a glide dislocation loop confined in a layer with thickness h also experiences pinning from bubbles in the layers (Figure 20a). The increase of stress $\Delta\tau$ due to He bubbles can be acquired by:

$$\Delta\tau = \tau_i \left(1 - \frac{L}{\sqrt{2}h}\right) \tag{29}$$

where L is the average obstacle spacing and τ_i is the average shear strength of obstacles. As the layer thickness h is small enough to ensure the interface crossing mechanism dominates in as-deposited

multilayers (Figure 20b), hardness has no increase after implantation, corresponding to $h < l$ in Equation (29); the model of CLS dominates in multilayers when the layer thickness h is large, bubbles inside layers become obstacles which can enhance the hardness, leading to irradiation-induced hardening, which can be described by Equation (29); the dislocation pile-up mechanism dominates in as-deposited multilayers as the layer thickness h is further increased, thus $\Delta\tau = \tau_i$ [96].

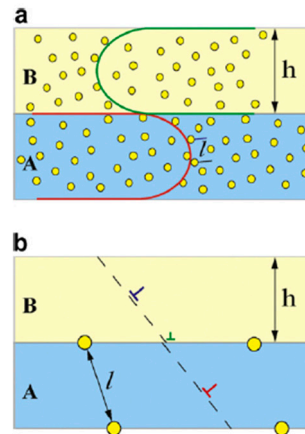


Figure 20. Schematic illustration of the length scale dependent deformation mechanism in multilayers after He irradiation. (a) When h is much larger than l , the deformation is via CLS with dislocations pinned by nanometer-scale bubbles. (b) When h is much smaller than l , the yield strength is determined by the crossing of single dislocation across interfaces, which contains a number of nanometer-scale He bubbles in the interface plane [96].

On the other hand, the introduction of abundant defects in materials at nanometer-length scale is one of the available strategies to achieve significantly enhancement of radiation tolerance [136]. Thus, NMMFs with large density of heterophase interfaces are evidently more resistant to radiation damage and have a higher He solubility [128]. The special role of heterogeneous interface in irradiation is often considered as follows. Firstly, NMMF nanostructured composites exhibit order-of-magnitude increases in He concentration. Helium implantation studies have shown that Cu/Nb nanocomposites have a higher He solubility than either Cu or Nb [137–139]. Secondly, the density of bubbles has been dramatically reduced in NMMFs. Although the He distribution is symmetrical along the interface, Figure 21 shows that obviously different bubble morphologies developed in the adjoining layers of Cu/Nb NMMF [128]. No bubbles were observed progressing into the Nb layer and the majority of bubbles were confined to the Cu side. Thirdly, the interface can effectively restrict the size of bubbles. Through an in-situ study, Yu et al. reported that 50 nm Ag/Ni NMMF has the smallest average defect size among Ag, Ni and their average value [136]. Fourthly, Helium capture ability mainly depends on the density of mismatch dislocation at the interface. Figure 22 shows the excellent agreement between misfit dislocation intersection densities at interfaces and the critical He concentrations per unit area of interface for a number of fcc/bcc NMMFs [140]. It must be pointed out that, except for He irradiation, for embrittlement induced by different radiations, the heterophase interfaces can act as effective sinks for defects from both strong obstacles such as interstitials, interstitial loops and stacking-fault tetrahedra, and relatively weak obstacles such as He bubbles. Therefore, NMMFs possessing excellent mechanical properties and having tunable interface structure and length scale, have stimulated increasingly interest in the research of radiation environment.

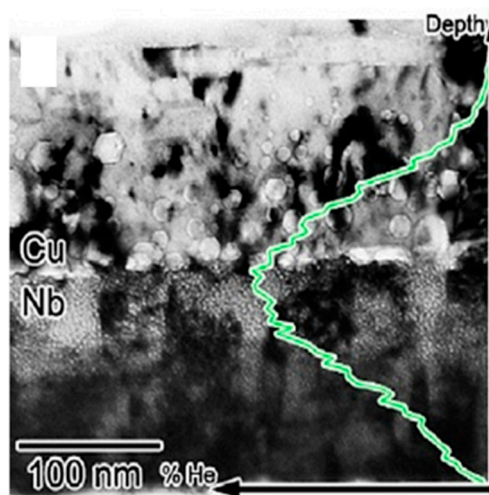


Figure 21. He bubbles in a Cu–Nb composite with $h = 120$ nm. The Nb layer (**bottom**) contains finely dispersed bubbles with diameter of 1–2 nm. The Cu layer (**top**) contains fewer, but larger He bubbles with a broad size distribution [21].

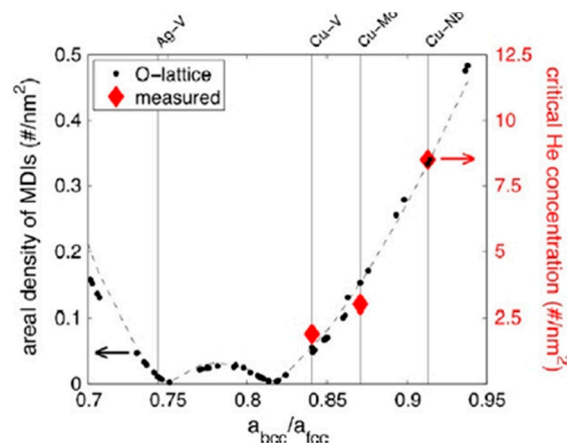


Figure 22. The excellent agreement between the densities of misfit dislocation intersection at interfaces and the critical He concentrations at interfaces for a number of fcc/bcc NMMFs. Red diamonds are measured values of the critical He concentrations [135].

Interfaces in NMMFs are good traps for implanted He, at the same time, they are also susceptible to He-induced embrittlement [140]. Thus, understanding the toughening mechanisms transition of NMMFs after irradiation is of great importance. After irradiation, the rate-controlling deformation mechanism of NC Ni [141] was identified to be the interaction of dislocations with irradiation-induced defects instead of traditional dislocations GBs interaction. Yet the related research for plastic deformation behavior of NMMFs after irradiation is limited. More studies are needed in this field, mainly including the effect of internal feature sizes, the distribution of the bubble and the crack interaction with defects in multilayer films.

4.5. Plasticity Instability

Strain localization is a common deformation-induced instability in NMMFs, which results in crack nucleation and subsequent fracture. Two instabilities are mainly reported. Firstly, in such layered materials, plasticity could localize in one of the constituent layers; secondly, the ductility is limited by the formation of localized shear bands in NMMFs.

4.5.1. Plasticity Localization

Owing to complex stress states beneath the indenter, the hardness obtained from instrumented indentation are always difficult to interpret the relative deformation extent between the two constituent layers. Finite element studies by Tan and Shen [142] showed that hardness is significantly large for a homogenous sample versus a multilayer sample with the same average properties. Using micropillar compression, experiment result (Figure 23) directly shows obvious extrusion of softer layers under the indenter. The deviation is proportional to the difference in individual layer yield strengths [32]. Wen et al. proposed a model of plastic deformation localization in soft layers which account for the low hardness in Ag/W NMMFs [98]. Plastic deformation only localized in soft layers at the initial stage of indentation, and hard layers only deflect to keep strain compatibility. Same test was performed on Ag/W NMMFs and a length scale dependent plasticity deformation mechanism is reported [40]. Plastic deformation of the Ag/W multilayers was accommodated by the two constituent layers together when the thickness of Ag layer is less than 20 nm, while the plastic deformation was mainly localized in Ag layers when thickness of Ag layer is larger than 20 nm.

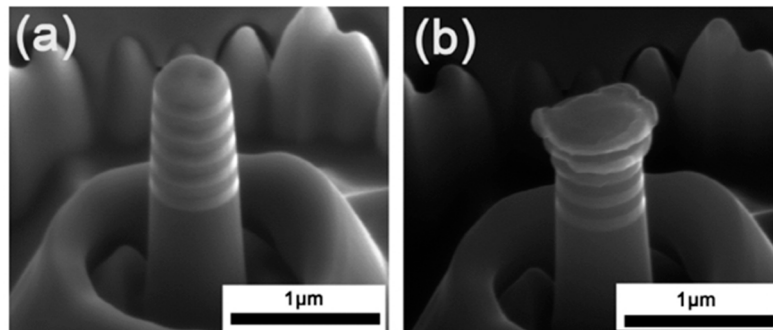


Figure 23. Pre-loading (a) and post-loading (b) scanning electron micrographs of micropillars of the Mg/Ti multilayer with $h = 100$ nm. The post-loading image indicates that under compression, the Mg layers (the layers of bright contrast) have been squeezed or extruded out between the mechanically rigid Ti layers [32].

4.5.2. Shear Banding Behavior

Shear banding behaviors were studied by many researchers and studies have been carried out to reveal mechanism of inhomogeneous flow in nanocrystalline, amorphous solids and nano-multilayers. The mechanisms of shear bands in NMMFs are attributed to the diminishing strain hardening ability and low strain rate sensitivity as the number of dislocations is limited. The hindered dislocation motion inside small grains is expected to make interfaces more active to accommodate plastic deformation, which leads to interface-related deformation behaviors, such as grain boundary sliding, grain rotation, etc. Experimental results of Au/Cu NMMFs [143] demonstrate that inhomogeneous shear banding becomes prevalent (Figure 24) when the h of the multilayered composite approach the nanometer range. Additionally, the width of shear bands decreases with the decrease of h while the maximum interface kink angles and pileup height increases with the decrease of h [143–145]. Along with further microscopic observation, two different types of interface morphologies are observed with the variation of h , which is corresponding to two shear-deformation behaviors [146]. On one hand, cooperative layer buckling induced shear banding in multilayers with h of 25 nm (Figure 25a). On the other hand, direct localized shearing go across a layer interface along a shear plane of the multilayers with h of 250 nm (Figure 25b). On a nanometer scale, buckling-assisted GB sliding leads to plastic instability of the multilayer, while on a submicron scale or more, dislocation plasticity dominates deformation instability of the multilayer (Figure 26 [88]). Wang et al. discovered that the plastic instabilities of Au/Ti multilayers under indentation changed from shear bands to layer buckling induced-delamination when the layer thickness was increased from 25 nm to 250 nm [16].

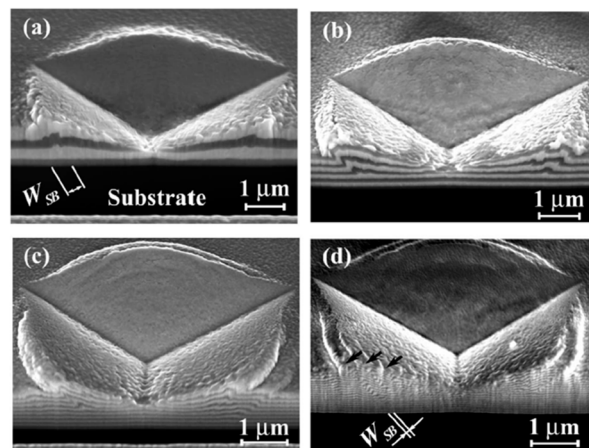


Figure 24. FIB cross-sectional views of the indents in the Au/Cu multilayers with h of (a) 250 nm, (b) 100 nm, (c) 50 nm, and (d) 25 nm [143].

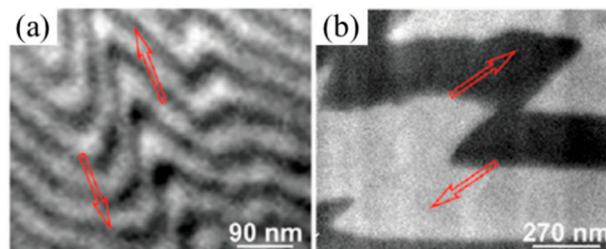


Figure 25. SEM cross-section view of two different deformation mechanisms corresponding to buckling-assisted layer rotation of (a) Au/Cu multilayer with $h = 25$ nm and dislocation plasticity-dominated shearing of (b) Au/Cu multilayer with $h = 250$ nm [146].

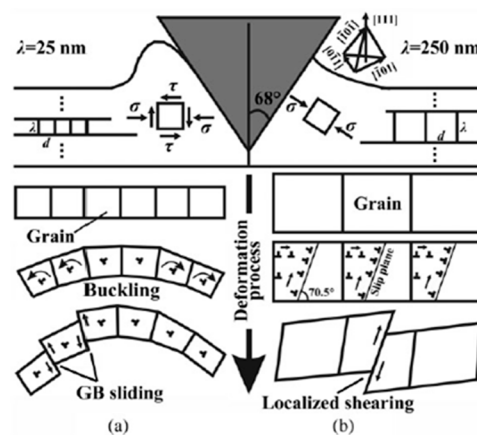


Figure 26. Schematic illustration of two different deformation mechanisms: (a) Au/Cu multilayer with $h = 25$ nm, which is corresponding to the elastic buckling-assisted GB sliding; and (b) Au/Cu multilayer with $h = 250$ nm, which is corresponding to the dislocation plasticity-dominated shearing [88].

The plastic deformation transition from plasticity localization (soft phase dominates) to shear banding deformation (co-deformation of both layers) in NMMFs has also been detected in micropillar compression tests. Mara [13] and Li [101] studied the deformation mode of Cu/Nb nanopillar, and found that, with h changing from 70 nm to 40 nm to 5 nm, the deformation mode changed from uniform extrusion of the soft layer gradually to a shear banding deformation and finally ($h = 5$ nm) to the highly localized shear fracture. The internal characteristics size related deformation process was also detected in Al/Pd NMMFs under pillar compression [147]. Zhang and coworkers [61,99] systematically investigated the effect of internal feature sizes (individual layer thickness h) and extrinsic

feature sizes (pillar diameter φ) on the deformation modes of Cu/Zr NMMFs and found that: with the decrease of the h , the deformation mode changed from the dislocation dominated symmetrical slip to shear localization and shear fracture; with the decrease of φ , the deformation mode changed from global shear to local shear. Figure 27 shows the deformation mode map (shear localization, shear + extrusion and extrusion) for NMMF.

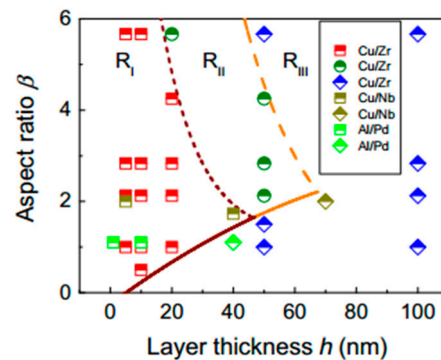


Figure 27. Deformation map for crystalline/crystalline nanolayered micropillars: shear localization in RI, shear + extrusion deformation in RII, extrusion and barreling deformation in RIII [61].

5. Conclusions and Future Developments

In this overview, we have emphasized the broad trends observed in the fracture properties of nanoscale metallic multilayer films, such as fracture toughness, wear resistance, adhesion energy, and plastic instability, which roughly summarize the development of NMMF in recent 10 years. A transition from bulk-like fracture behavior to one controlled by individual dislocation and interface-mediated fracture has been reviewed. Interface structure and length scale are believed to be two important factors deciding the fracture response. In sharp contrast to tough monolithic crystalline metals, the presence of interfaces enables the very high strength associated with the multilayered structure. Accordingly, through properly tailoring the internal features (length scale and interface structure), an optimized combination of fracture toughness and strength can be obtained, which runs counter to the popular belief that increasing the strength leads to a decrease in the fracture toughness in materials. This finding is potentially able to explain effectively ‘structure–properties’ relationships that are used to advantage in multilayered composites, where the microstructure can be tailored with the goal of achieving a high density of fcc/fcc coherent interfaces [15]. Hopefully, the theoretical analyses and available experimental results can provide further impetus for understanding the nanoscale damage of multilayers, with which it is possible to artificially control the constituent phases or dimension configurations to achieve target performance in technological applications.

While there are still many key issues that remain puzzling. Their resolution would undoubtedly lead to improved fracture properties and superior understanding of the deformation map for NMMFs. In the following, we list a few questions with which we are concerned, which may shed light on further development.

1. The length scale-dependent toughening map [15] is mainly build on an integrated interface which acts as effective barriers for crack propagation, and there is largely ignored interdiffusion at the interfaces, especially at small h and in multilayers with negative heat of mixing [148–150]. The formation of alloys and amorphous is a result of interface diffusion [95,151,152], which should be considered in building the deformation map for NMMFs. For $h < 1$ nm, even a small amount of interdiffusion may have a pronounced effect on interface stress and strength [148,153]. Additionally, residual stress in the layers, e.g., growth stress in NMMFs could also be important in influencing the toughening model [154].

2. Plastic deformation of NMMFs has been described using various mechanisms with varying levels of success. While the majority of the mechanisms focus on the NMMFs with equal individual

layer thickness (modulation ratio $\eta = 1$), few works concern NMMFs with varying modulation ratios. Under certain conditions, such as modulation-induced structure transition (Section 2.2.1) and length-scale-induced toughening (Section 4.1), it is not only interesting, but also of practical requirement to establish more comprehensive models for exploring the size effect.

3. Recent studies show that interface structure also plays an important role in shear instability in NMMFs. Dislocation transmission favors the formation of crystallographic band, whereas dislocations do not transmit which cause interface tilting and are associated with shear band formation [155]. It is also argued that the interface with low shear strength and strong barriers for slip transmission indicates a new mechanism for shear banding and fracture [13]. However, early studies show that fcc Cu/bcc Cr multilayers can be more effective in resisting shear-band deformation than the Cu/Au multilayers, as a result of the higher resistance of the Cu/Cr interface to dislocation transmission [156]. More sound explanations are needed about whether the interface structure plays an important role in the shear banding and subsequent shear fracture processes in NMMFs or not.

After all, the fracture properties of nanoscale metallic multilayer films are closely related to the interfaces. At present, there are abundant research opportunities in the area regarding the strengthening mechanisms, except the unresolved issues we outlined, the fatigue, creep, fracture, and irradiation failure mechanics of multilayer are still in the data accumulation stage. An in-depth understanding of this will continue to flourish and seems to be in sight.

Author Contributions: Q.Z. conceived and designed the contents; Y.R. and Y.D. wrote Section 2; D.H. and W.H. wrote Section 3; and all authors participated in discussing and finalizing the paper.

Funding: The research is funded by the Natural Science Foundation of China (no. 51801161), the Initiative Postdocs Supporting Program (no. BX20180256) and the Fundamental Research Funds for the Central Universities.

Acknowledgments: The authors would like to thank Ping Huang and Fei Wang at Xi'an Jiaotong University for helpful guidance.

Conflicts of Interest: The authors declare no conflict of interest.

Nomenclature

A	The projected contact area of the hardness impression (nm^2)
A_c	The area of the crack (nm^2)
A_{Su}	The average cross-sectional area of the substrate pillar.
A_0	The cross-sectional area at half initial height of the pillar (nm^2)
a	Atomic radiuses (nm)
\bar{a}	Mean values of the atomic diameter (nm)
a^*	The crack radius (nm)
b	Burgers vector (nm)
C	The compliance of the film (nm)
d_b	The diameter of bubbles (nm)
d_i	The diameter of interstitial loops (nm)
E	The Young's modulus
E_{eff}	The effective modulus (GPa)
E_f	Respective modulus of film (GPa)
$E_{measured}$	The measured modulus of the tapered NMMFs (GPa)
E_s	Respective modulus of substrate (GPa)
E_{Su}	The modulus of the substrate pillar (GPa)
E_{total}	Young's modulus of the film/substrate system in uniaxial tension (GPa)
ΔF	The measured force difference (GPa)
f	Volume fraction
ΔG	The allotropic free energy change per unit volume of the constituent in multilayers (J m^{-3})
Δg	Specific free energy normalized by the area of the interface ($\text{J}\cdot\text{m}^{-2}$)
H	Hardness (GPa)
H_{max}	Peak hardness (GPa)

H_{rom}	Rule-of-mixtures hardness (GPa)
\overline{H}_m	Mean values of the melting enthalpy (kJ/mol)
h	Individual layer thickness (nm)
h_c	The critical thickness to form perfect coherent interfaces (nm)
h_f	The film thickness (nm)
h_0	The penetration depth (nm)
h_φ	The layer thickness measured parallel to the glide plane (nm)
K_{app}	The far field mode I stress intensity ($\text{MPa}\cdot\text{m}^{1/2}$)
K_{IC}	The fracture toughness ($\text{MPa}\cdot\text{m}^{1/2}$)
k_B	The Boltzmann constant
L	The distance between source and obstacle (nm)
L_0	Half initial height of the pillar (nm)
L_p	The final height of the pillar (nm)
L_{Su}	The total length of the substrate pillar (nm)
l	Half of the buckle width (nm)
M	The Taylor factor
N_d	The defects density across the radiation damage region
n	The equilibrium number of dislocations
P	The load in compression test (mN)
P_{max}	Peak load in nanoindentation (mN)
Q	The activation energy (J)
R	The ideal gas constant ($\text{J}/(\text{mol}\cdot\text{K})$)
r	Crack length (nm)
r_0	The effective core radius, the radius at the top of the pillar (nm)
r_d	The radius of the defect cluster (nm)
S	Contact stiffness (N/m)
s	The equilibrium spacing of misfit dislocations (nm)
\overline{S}_{vib}	Mean values of the vibration part of the overall melting entropy (kJ/mol)
T	The absolute temperature (K)
t	Time (s)
U_e	The elastic energy (J)
V	The plastic volume displaced by the indenter (nm^3)
\overline{V}_m	Mean values of the molar volumes of corresponding substances consisting of interfaces
α	The Saada's constant
α_1, α_2	Two Dundurs' parameters
β	A constant which depends on the geometry of the indenter
γ	Surface or interface energy ($\text{J}\cdot\text{m}^{-2}$)
γ_c	The coherent interface energy ($\text{J}\cdot\text{m}^{-2}$)
γ_{in}	The incoherent interface energy ($\text{J}\cdot\text{m}^{-2}$)
γ_s	Stacking fault energy ($\text{J}\cdot\text{m}^{-2}$)
$\Delta\gamma$	Change in interfacial free energy ($\text{J}\cdot\text{m}^{-2}$)
Γ	Interfacial adhesion energy
Γ_{AB}	Surface energy mismatch
ε	The misfit strain
ε_c	Macroscopic strain
ε_0	The in-plane plastic strain
ε_T	The true strain in flat punch compression
σ_T	The true stress in flat punch compression (GPa)
λ	The bilayer thickness (nm)
μ	Shear modulus (GPa)
u_{tot}	The total displacement in pillar compression (nm)
μ^*	The mean shear modulus (GPa)
ν	The Poisson ratio
ζ	Steady-state energy release rate ($\text{J}\cdot\text{m}^{-2}$)
ζ_c	The critical energy release rate ($\text{J}\cdot\text{m}^{-2}$)
δ	Lattice mismatch

δ^*	Buckle height (nm)
σ	Uniaxial stress, flow strength (GPa)
σ_0	The intrinsic stress yield strength (GPa)
σ_y	The yield strength (GPa)
σ_{total}	The yield strength of the film/substrate system (GPa)
σ_r	The residual stress in the film (GPa)
σ_s	The yield strength of the substrate (GPa)
σ_{max}	The maximum yield stress (GPa)
τ	Applied shear stress (GPa)
τ_0	Lattice friction stress (GPa)
τ_i	The average shear strength of obstacles (GPa)
$\Delta\tau$	The increase of stress due to He bubbles (GPa)
ϕ	The angle of inclination of the slip plane to the interface
φ_c	Half of a critical bow-out angle between lines of a dislocation cutting an obstacle

List of Acronyms

bcc	Body-centered cubic
CLS	Confined layer slip
ED	Electrodeposition
fcc	Face-centered cubic
GB	Grain boundary
hcp	Hexagonal close-packed
NMMFs	Nanoscale metallic multilayer films
PVD	Physical vapor deposition

References

- Misra, A.; Verdier, M.; Lu, Y.C.; Kung, H.; Mitchell, T.E.; Nastasi, M. Structure and mechanical properties of Cu-X (X = Nb, Cr, Ni) nanolayered composites. *Scr. Mater.* **1998**, *39*, 555–560. [[CrossRef](#)]
- Damadam, M.; Shao, S.; Ayoub, G.; Zbib, H.M. Recent advances in modeling of interfaces and mechanical behavior of multilayer metallic/ceramic composites. *J. Mater. Sci.* **2018**, *53*, 5604–5617. [[CrossRef](#)]
- Misra, A.; Kung, H.; Embury, J.D. Preface to the viewpoint set on: Deformation and stability of nanoscale metallic multilayers. *Scr. Mater.* **2004**, *50*, 707–710. [[CrossRef](#)]
- Bufford, D.; Bi, Z.; Jia, Q.X.; Wang, H. Nanotwins and stacking faults in high-strength epitaxial Ag/Al multilayer films. *Appl. Phys. Lett.* **2012**, *101*, 27. [[CrossRef](#)]
- Mara, N.A.; Bhattacharyya, D.; Dickerson, P.; Hoagland, R.G.; Misra, A. Deformability of ultrahigh strength 5 nm Cu/Nb nanolayered composites. *Appl. Phys. Lett.* **2008**, *92*, 1765. [[CrossRef](#)]
- Mara, N.A.; Bhattacharyya, D.; Dickerson, P.O.; Hoagland, R.G.; Misra, A. Ultrahigh strength and ductility of Cu-Nb nanolayered composites. In *Materials Science Forum*; Trans Tech Publications: Zürich, Switzerland, 2009; pp. 647–653.
- Misra, A.; Zhang, X.; Hammon, D.; Hoagland, R.G. Work hardening in rolled nanolayered metallic composites. *Acta Mater.* **2005**, *53*, 221–226. [[CrossRef](#)]
- Zhang, J.Y.; Zhang, X.; Wang, R.H.; Lei, S.Y.; Zhang, P.; Niu, J.J. Length-scale-dependent deformation and fracture behavior of Cu/X (X = Nb, Zr) multilayers: The constraining effects of the ductile phase on the brittle phase. *Acta Mater.* **2011**, *59*, 7368–7379. [[CrossRef](#)]
- Zhou, Q.; Xie, J.Y.; Wang, F.; Huang, P.; Xu, K.W.; Lu, T.J. The mechanical behavior of nanoscale metallic multilayers: A survey. *Acta Mech. Sin.* **2015**, *31*, 319–337. [[CrossRef](#)]
- Li, Y.; Zhou, Q.; Zhang, S.; Huang, P.; Xu, K.; Wang, F. On the role of weak interface in crack blunting process in nanoscale layered composites. *Appl. Surf. Sci.* **2018**, *433*, 957–962. [[CrossRef](#)]
- Wang, J.; Zhou, Q.; Shao, S.; Misra, A. Strength and plasticity of nanolaminated materials. *Mater. Res. Lett.* **2016**, *5*, 1–19. [[CrossRef](#)]
- Zhang, J.Y.; Liu, G.; Zhang, X.; Zhang, G.J.; Sun, J.; Ma, E. A maximum in ductility and fracture toughness in nanostructured Cu/Cr multilayer films. *Scr. Mater.* **2010**, *62*, 333–336. [[CrossRef](#)]
- Mara, N.A.; Bhattacharyya, D.; Hirth, J.P.; Dickerson, P. Mechanism for shear banding in nanolayered composites. *Appl. Phys. Lett.* **2010**, *97*, 2935. [[CrossRef](#)]

14. Carpenter, J.S.; Misra, A.; Anderson, P.M. Achieving maximum hardness in semi-coherent multilayer thin films with unequal layer thickness. *Acta Mater.* **2012**, *60*, 2625–2636. [[CrossRef](#)]
15. Zhou, Q.; Zhang, S.; Wei, X.; Wang, F.; Huang, P.; Xu, K. Improving the crack resistance and fracture toughness of Cu/Ru multilayer thin films via tailoring the individual layer thickness. *J. Alloys Compd.* **2018**, *742*, 45–53. [[CrossRef](#)]
16. Wang, D.; Kups, T.; Schawohl, J.; Schaaf, P. Deformation behavior of Au/Ti multilayers under indentation. *J. Mater. Sci. Mater. Electron.* **2012**, *23*, 1077–1082. [[CrossRef](#)]
17. Zhu, X.Y.; Liu, X.J.; Zong, R.L.; Zeng, F.; Pan, F. Microstructure and mechanical properties of nanoscale Cu/Ni multilayers. *Mater. Sci. Eng. A* **2010**, *527*, 1243–1248. [[CrossRef](#)]
18. Kang, K.; Wang, J.; Beyerlein, I.J. Atomic structure variations of mechanically stable fcc-bcc interfaces. *J. Appl. Phys.* **2012**, *111*, 1673. [[CrossRef](#)]
19. Li, N.; Wang, J.; Huang, J.Y.; Misra, A.; Zhang, X. In situ tem observations of room temperature dislocation climb at interfaces in nanolayered Al/Nb composites. *Scr. Mater.* **2010**, *4*, 363–366. [[CrossRef](#)]
20. Chen, Y.; Yu, K.Y.; Wang, H.; Chen, J.; Zhang, X. Stacking fault and partial dislocation dominated strengthening mechanisms in highly textured Cu/Co multilayers. *Int. J. Plast.* **2013**, *49*, 152–163.
21. Ham, B.; Zhang, X. High strength Mg/Nb nanolayer composites. *Mater. Sci. Eng. A* **2011**, *528*, 2028–2033. [[CrossRef](#)]
22. Banerjee, R.; Zhang, X.D.; Dregia, S.A.; Fraser, H.L. Phase stability in Al/Ti multilayers. *Acta Mater.* **1999**, *47*, 1153–1161. [[CrossRef](#)]
23. Redfield, A.C.; Zangwill, A.M. Stacking sequences in close-packed metallic superlattices. *Phys. Rev. B* **1986**, *34*, 1378–1380. [[CrossRef](#)]
24. Bruinsma, R.; Zangwill, A. Structural transitions in epitaxial overlayers. *J. Phys.* **1986**, *47*, 2055–2073. [[CrossRef](#)]
25. Dregia, S.A.; Banerjee, R.; Fraser, H.L. Polymorphic phase stability in thin multilayers. *Scr. Mater.* **1998**, *39*, 217–223. [[CrossRef](#)]
26. Li, J.C.; Liu, W.; Jiang, Q. Bi-phase transition diagrams of metallic thin multilayers. *Acta Mater.* **2005**, *53*, 1067–1071. [[CrossRef](#)]
27. Zhang, J.Y.; Zhang, P.; Zhang, X.; Wang, R.H.; Liu, G.; Zhang, G.J. Mechanical properties of fcc/fcc Cu/Nb nanostructured multilayers. *Mater. Sci. Eng. A* **2012**, *545*, 118–122. [[CrossRef](#)]
28. Xie, J.Y.; Wang, F.; Huang, P.; Lu, T.J.; Zhang, L.F.; Xu, K.W. Structure transformation and coherent interface in large lattice-mismatched nanoscale multilayers. *J. Nanomater.* **2013**, *12*, 71. [[CrossRef](#)]
29. Wei, Q.M.; Liu, X.Y.; Misra, A. Observation of continuous and reversible bcc–fcc phase transformation in Ag/V multilayers. *Appl. Phys. Lett.* **2011**, *98*, 4817. [[CrossRef](#)]
30. Chen, Y.; Liu, Y.; Sun, C.; Yu, K.Y.; Song, M.; Wang, H. Microstructure and strengthening mechanisms in Cu/Fe multilayers. *Acta Mater.* **2012**, *60*, 6312–6321. [[CrossRef](#)]
31. Wang, J.; Hoagland, R.G.; Misra, A. Phase transition and dislocation nucleation in Cu-Nb layered composites during physical vapor deposition. *J. Mater. Res.* **2011**, *23*, 1009–1014. [[CrossRef](#)]
32. Lu, Y.Y.; Kotoka, R.; Ligda, J.P.; Cao, B.B.; Yarmolenko, S.N.; Schuster, B.E. The microstructure and mechanical behavior of Mg/Ti multilayers as a function of individual layer thickness. *Acta Mater.* **2014**, *63*, 216–231. [[CrossRef](#)]
33. Freund, L.B.; Suresh, S. *Thin Film Materials: Stress, Defect Formation, and Surface Evolution*; Cambridge University Press: Cambridge, UK, 2003.
34. Matthews, J.W.; Blakeslee, A.E. Defects in epitaxial multilayers. *J. Cryst. Growth* **1974**, *32*, 118–125.
35. Misra, A.; Verdier, M.; Kung, H.; Embury, J.D.; Hirth, J.P. Erratum deformation mechanism maps for polycrystalline metallic multilayers. *Scr. Mater.* **1999**, *41*, 973–979. [[CrossRef](#)]
36. Jennings, A.T.; Li, J.; Greer, J.R. Emergence of strain-rate sensitivity in Cu nanopillars: Transition from dislocation multiplication to dislocation nucleation. *Acta Mater.* **2011**, *59*, 5627–5637. [[CrossRef](#)]
37. Wen, S.P.; Zeng, F.; Pan, F.; Nie, Z.R. The influence of grain morphology on indentation deformation characteristic of metallic nano-multilayers. *Mater. Sci. Eng. A* **2009**, *526*, 166–170. [[CrossRef](#)]
38. Oliver, W.C.; Pharr, G.M. An improved technique for determining hardness and elastic modulus using load and displacement sensing indentation. *J. Mater. Res.* **1992**, *7*, 1564–1583. [[CrossRef](#)]
39. Wen, S.P.; Zeng, F.; Gao, Y.; Pan, F. Microstructure and nanoindentation investigation of magnetron sputtering Ag/Co multilayers. *Surf. Coat. Technol.* **2006**, *201*, 1262–1266. [[CrossRef](#)]

40. Zhou, Q.; Wang, F.; Huang, P.; Xu, K.W. Strain rate sensitivity and related plastic deformation mechanism transition in nanoscale Ag/W multilayers. *Thin Solid Films* **2014**, *571*, 253–259. [[CrossRef](#)]
41. Wen, S.P.; Zeng, F.; Gao, Y.; Pan, F. Indentation creep behavior of nano-scale Ag/Co multilayers. *Scr. Mater.* **2006**, *55*, 187–190. [[CrossRef](#)]
42. Zhu, X.Y.; Luo, J.T.; Zeng, F.; Pan, F. Microstructure and ultrahigh strength of nanoscale Cu/Nb multilayers. *Thin Solid Films* **2011**, *520*, 818–823. [[CrossRef](#)]
43. Zhu, X.Y.; Liu, X.J.; Zeng, F.; Pan, F. Room temperature nanoindentation creep of nanoscale Ag/Fe multilayers. *Mater. Lett.* **2010**, *64*, 53–56. [[CrossRef](#)]
44. Pharr, G.M. Measurement of mechanical properties by ultra-low load indentation. *Mater. Sci. Eng. A* **1998**, *253*, 151–159. [[CrossRef](#)]
45. Doerner, M.F.; Nix, W.D. A method for interpreting the data form depth-sensing indentation instruments. *J. Mater. Res.* **1986**, *1*, 601–609. [[CrossRef](#)]
46. Zhang, J.Y.; Zhang, X.; Liu, G.; Zhang, G.J.; Sun, J. Dominant factor controlling the fracture mode in nanostructured Cu/Cr multilayer films. *Mater. Sci. Eng. A* **2011**, *528*, 2982–2987. [[CrossRef](#)]
47. Zhang, J.Y.; Zhang, X.; Liu, G.; Zhang, G.J.; Sun, J. Scaling of the ductility with yield strength in nanostructured Cu/Cr multilayer films. *Scr. Mater.* **2010**, *63*, 101–104. [[CrossRef](#)]
48. Hu, K.; Xu, L.J.; Cao, Y.Q.; Pan, G.J.; Cao, Z.H.; Meng, X.K. Modulating individual thickness for optimized combination of strength and ductility in Cu/Ru multilayer films. *Mater. Lett.* **2013**, *107*, 303–306. [[CrossRef](#)]
49. Niu, R.M.; Liu, G.; Wang, C.; Zhang, G.; Ding, X.D.; Sun, J. Thickness dependent critical strain in submicron Cu films adherent to polymer substrate. *Appl. Phys. Lett.* **2007**, *90*, 87. [[CrossRef](#)]
50. Yu, D.Y.W.; Spaepen, F. The yield strength of thin copper films on kapton. *J. Appl. Phys.* **2004**, *95*, 2991–2997. [[CrossRef](#)]
51. Avilés, F.; Llanes, L.; Oliva, A.I. Elasto-plastic properties of gold thin films deposited onto polymeric substrates. *J. Mater. Sci.* **2009**, *44*, 2590–2598. [[CrossRef](#)]
52. Wu, K.; Zhang, J.Y.; Liu, G.; Zhang, P.; Cheng, P.M.; Li, J. Buckling behaviors and adhesion energy of nanostructured Cu/X (X = Nb, Zr) multilayer films on a compliant substrate. *Acta Mater.* **2013**, *61*, 7889–7903. [[CrossRef](#)]
53. Beuth, J.L., Jr. Cracking of thin bonded films in residual tension. *J. Solids Struct.* **1992**, *29*, 1657–1675. [[CrossRef](#)]
54. Dundurs, J. Discussion: “Edge-bonded dissimilar orthogonal elastic wedges under normal and shear loading”. *J. Appl. Mech.* **1969**, *36*, 460–466.
55. Was, G.S.; Foecke, T. Deformation and fracture in microlaminates. *Thin Solid Films* **1996**, *286*, 1–31. [[CrossRef](#)]
56. Mata, M.; Anglada, M.; Alcalá, J. Contact deformation regimes around sharp indentations and the concept of the characteristic strain. *J. Mater. Res.* **2002**, *17*, 964–976. [[CrossRef](#)]
57. Carpenter, J.S.; Misra, A.; Uchic, M.D.; Anderson, P.M. Strain rate sensitivity and activation volume of Cu/Ni metallic multilayer thin films measured via micropillar compression. *Appl. Phys. Lett.* **2012**, *101*, 051901. [[CrossRef](#)]
58. Uchic, M.D.; Dimiduk, D.M.; Florando, J.N.; Nix, W.D. Sample dimensions influence strength and crystal plasticity. *Science* **2004**, *305*, 986. [[CrossRef](#)] [[PubMed](#)]
59. Uchic, M.D.; Dimiduk, D.M. A methodology to investigate size scale effects in crystalline plasticity using uniaxial compression testing. *Mater. Sci. Eng. A* **2005**, *400*, 268–278. [[CrossRef](#)]
60. Zhang, J.Y.; Wang, Y.Q.; Wu, K.; Zhang, P.; Liu, G.; Zhang, G.J. Strain rate sensitivity of nanolayered Cu/X (X = Cr, Zr) micropillars: Effects of heterophase interface/twin boundary. *Mater. Sci. Eng. A* **2014**, *612*, 28–40. [[CrossRef](#)]
61. Zhang, J.Y.; Lei, S.; Niu, J.; Liu, Y.; Liu, G.; Zhang, X. Intrinsic and extrinsic size effects on deformation in nanolayered Cu/Zr micropillars: From bulk-like to small-volume materials behavior. *Acta Mater.* **2012**, *60*, 4054–4064. [[CrossRef](#)]
62. Volkert, C.A.; Lilleodden, E.T.; Kramer, D.; Weissmüller, J. Approaching the theoretical strength in nanoporous Au. *Appl. Phys. Lett.* **2006**, *89*, 061920. [[CrossRef](#)]
63. Greer, J.R.; Oliver, W.C.; Nix, W.D. Corrigendum to “size dependence in mechanical properties of gold at the micron scale in the absence of strain gradients”. *Acta Mater.* **2006**, *54*, 1821–1830.
64. Dimiduk, D.M.; Uchic, M.D.; Parthasarathy, T.A. Size-affected single-slip behavior of pure nickel microcrystals. *Acta Mater.* **2005**, *53*, 4065–4077. [[CrossRef](#)]

65. Han, S.M.; Phillips, M.A.; Nix, W.D. Study of strain softening behavior of Al–AlSc multilayers using microcompression testing. *Acta Mater.* **2009**, *57*, 4473–4490. [[CrossRef](#)]
66. Singh, D.R.P.; Chawla, N.; Tang, G.; Shen, Y.L. Micropillar compression of Al/SiC nanolaminates. *Acta Mater.* **2010**, *58*, 6628–6636. [[CrossRef](#)]
67. Li, Y.P.; Zhang, G.P. On plasticity and fracture of nanostructured Cu/X (X = Au, Cr) multilayers: The effects of length scale and interface/boundary. *Acta Mater.* **2010**, *58*, 3877–3887. [[CrossRef](#)]
68. Jaeger, G.; Endler, I.; Heilmaier, M.; Bartsch, K.; Leonhardt, A. A new method of determining strength and fracture toughness of thin hard coatings. *Thin Solid Films* **2000**, *377*, 382–388. [[CrossRef](#)]
69. Bellido-González, V.; Stefanopoulos, N.; Deguilhen, F. Friction monitored scratch adhesion testing. *Surf. Coat. Technol.* **1995**, *74–75*, 884–889. [[CrossRef](#)]
70. Li, X.; Bhushan, B. Micro/nanomechanical and tribological characterization of ultrathin amorphous carbon coatings. *J. Mater. Res.* **1999**, *14*, 2328–2337. [[CrossRef](#)]
71. Sundararajan, S.; Bhushan, B. Development of a continuous microscratch technique in an atomic force microscope and its application to study scratch resistance of ultrathin hard amorphous carbon coatings. *J. Mater. Res.* **2001**, *16*, 437–445. [[CrossRef](#)]
72. Niu, E.W.; Li, L.; Lv, G.H.; Chen, H.; Li, X.Z.; Yang, X.Z. Characterization of Ti–Zr–N films deposited by cathodic vacuum arc with different substrate bias. *Appl. Surf. Sci.* **2008**, *254*, 3909–3914. [[CrossRef](#)]
73. Johnson, M.C.; Lew, C.M.; Yan, Y.; Wang, J. Hydrophobicity-dependent friction and wear of spin-on zeolite thin films. *Scr. Mater.* **2008**, *58*, 41–44. [[CrossRef](#)]
74. Wei, G.; Scharf, T.W.; Zhou, J.N.; Huang, F.; Weaver, M.L.; Barnard, J.A. Nanotribology studies of Cr, Cr₂N and CrN thin films using constant and ramped load nanoscratch techniques. *Surf. Coat. Technol.* **2001**, *146*, 357–362. [[CrossRef](#)]
75. Panjan, P.; Čekada, M.; Navinšek, B. A new experimental method for studying the cracking behaviour of PVD multilayer coatings. *Surf. Coat. Technol.* **2003**, *174*, 55–62. [[CrossRef](#)]
76. Wen, S.P.; Zong, R.L.; Zeng, F.; Guo, S.; Pan, F. Nanoindentation and nanoscratch behaviors of Ag/Ni multilayers. *Appl. Surf. Sci.* **2009**, *255*, 4558–4562. [[CrossRef](#)]
77. Blum, W. The structure and properties of alternately electrodeposited metals. *Trans. Am. Electrochem. Soc.* **1921**, *40*, 307–320.
78. Misra, A.; Hirth, J.P.; Hoagland, R.G. Length-scale-dependent deformation mechanisms in incoherent metallic multilayered composites. *Acta Mater.* **2005**, *53*, 4817–4824. [[CrossRef](#)]
79. Yahalom, J.; Tessier, D.F.; Timsit, R.S.; Rosenfeld, A.M.; Mitchell, D.F.; Robinson, P.T. Structure of composition-modulated Cu/Ni thin films prepared by electrodeposition. *J. Mater. Res.* **1989**, *4*, 755–758. [[CrossRef](#)]
80. Liu, Y.; Bufford, D.; Wang, H.; Sun, C.; Zhang, X. Mechanical properties of highly textured Cu/Ni multilayers. *Acta Mater.* **2011**, *59*, 1924–1933. [[CrossRef](#)]
81. Misra, A.; Hirth, J.P.; Kung, H. Single-dislocation-based strengthening mechanisms in nanoscale metallic multilayers. *Philos. Mag. A* **2002**, *82*, 2935–2951. [[CrossRef](#)]
82. Tench, D.M. Tensile properties of nanostructured Ni–Cu multilayered materials prepared by electrodeposition. *J. Electrochem. Soc.* **1991**, *138*, 3757–3758. [[CrossRef](#)]
83. Cammarata, R.C.; Schlesinger, T.E.; Kim, C.; Qadri, S.B.; Edelstein, A.S. Nanoindentation study of the mechanical properties of copper–nickel multilayered thin films. *Appl. Phys. Lett.* **1990**, *56*, 1862–1864. [[CrossRef](#)]
84. Rao, S.I.; Hazzledine, P.M. Atomistic simulations of dislocation–interface interactions in the Cu–Ni multilayer system. *Philos. Mag. A* **2000**, *80*, 2011–2040. [[CrossRef](#)]
85. Hoagland, R.G.; Mitchell, T.E.; Hirth, J.P.; Kung, H. On the strengthening effects of interfaces in multilayer fcc metallic composites. *Philos. Mag. A* **2002**, *82*, 643–664. [[CrossRef](#)]
86. Wang, F.; Zhang, L.F.; Huang, P.; Xie, J.Y.; Lu, T.J.; Xu, K.W. Microstructure and Flow Stress of Nanoscale Cu/Nb Multilayers. *J. Nanomater.* **2013**, *55*. [[CrossRef](#)]
87. Mara, N.A.; Bhattacharyya, D.; Hoagland, R.G.; Misra, A. Tensile behavior of 40 nm Cu/Nb nanoscale multilayers. *Scr. Mater.* **2008**, *58*, 874–877. [[CrossRef](#)]
88. Li, Y.P.; Zhu, X.F.; Zhang, G.P.; Tan, J.; Wang, W.; Wu, B. Investigation of deformation instability of Au/Cu multilayers by indentation. *Philos. Mag.* **2010**, *90*, 3049–3067. [[CrossRef](#)]

89. Fu, E.G.; Li, N.; Misra, A.; Hoagland, R.G.; Wang, H.; Zhang, X. Mechanical properties of sputtered Cu/W and Al/Nb multilayer films. *Mater. Sci. Eng. A* **2008**, *493*, 283–287. [[CrossRef](#)]
90. Wen, S.P.; Zong, R.L.; Zeng, F.; Gao, Y.; Pan, F. Evaluating modulus and hardness enhancement in evaporated Cu/W multilayers. *Acta Mater.* **2007**, *55*, 345–351. [[CrossRef](#)]
91. Huang, P.; Wang, F.; Xu, M.; Lu, T.J.; Xu, K.W. Strain rate sensitivity of unequal grained nano-multilayers. *Mater. Sci. Eng. A* **2011**, *528*, 5908–5913. [[CrossRef](#)]
92. Zhang, J.Y.; Liu, Y.; Chen, J.; Chen, Y.; Liu, G.; Zhang, X. Mechanical properties of crystalline Cu/Zr and crystal–amorphous Cu/Cu–Zr multilayers. *Mater. Sci. Eng. A* **2012**, *552*, 392–398. [[CrossRef](#)]
93. Wen, S.P.; Zong, R.L.; Zeng, F.; Gao, Y.; Pan, F. Nanoindentation investigation of the mechanical behaviors of nanoscale Ag/Cu multilayers. *J. Mater. Res.* **2007**, *22*, 3423–3431. [[CrossRef](#)]
94. Geisler, H.; Schweitz, K.O.; Chevallier, J.; Böttiger, J.; Samwer, K. Hardness enhancement and elastic modulus behaviour in sputtered Ag/Ni multilayers with different modulation wavelengths. *Philos. Mag. A* **1999**, *79*, 485–500. [[CrossRef](#)]
95. Lai, W.S.; Yang, M.J. Observation of largely enhanced hardness in nanomultilayers of the Ag–Nb system with positive enthalpy of formation. *Appl. Phys. Lett.* **2007**, *90*, 217. [[CrossRef](#)]
96. Wei, Q.M.; Li, N.; Mara, N.; Nastasi, M.; Misra, A. Suppression of irradiation hardening in nanoscale V/Ag multilayers. *Acta Mater.* **2011**, *59*, 6331–6340. [[CrossRef](#)]
97. Zhu, X.Y.; Liu, X.J.; Zeng, F.; Pan, F. Microstructure and nanoindentation hardness of Ag/Fe multilayers. *Trans. Nonferrous Met. Soc. China* **2010**, *20*, 110–114. [[CrossRef](#)]
98. Wen, S.P.; Zong, R.L. Influence of plasticity mismatch and porosity on mechanical behavior of nanoscale Ag/W multilayers. *Mater. Sci. Eng. A* **2007**, *457*, 38–43. [[CrossRef](#)]
99. Zhang, J.Y.; Lei, S.; Liu, Y.; Niu, J.J.; Chen, Y.; Liu, G. Length scale-dependent deformation behavior of nanolayered Cu/Zr micropillars. *Acta Mater.* **2012**, *60*, 1610–1622. [[CrossRef](#)]
100. Kim, Y.; Budiman, A.S.; Baldwin, J.K.; Mara, N.A.; Misra, A.; Han, S.M. Microcompression study of Al–Nb nanoscale multilayers. *J. Mater. Res.* **2012**, *27*, 592–598. [[CrossRef](#)]
101. Li, N.; Mara, N.A.; Wang, Y.Q.; Nastasi, M.; Misra, A. Compressive flow behavior of Cu thin films and Cu/Nb multilayers containing nanometer-scale helium bubbles. *Scr. Mater.* **2011**, *64*, 974–977. [[CrossRef](#)]
102. Huang, H.; Spaepen, F. Tensile testing of free-standing Cu, Ag and Al thin films and Ag/Cu multilayers. *Acta Mater.* **2000**, *48*, 3261–3269. [[CrossRef](#)]
103. Lehoczyk, S.L. Strength enhancement in thin-layered Al–Cu laminates. *J. Appl. Phys.* **1978**, *49*, 5479–5485. [[CrossRef](#)]
104. Josell, D.; Heerden, D.V.; Read, D.; Shechtman, J.B.D. Tensile testing low density multilayers: Aluminum/titanium. *J. Mater. Res.* **1998**, *13*, 2902–2909. [[CrossRef](#)]
105. Aydiner, C.C.; Brown, D.W.; Mara, N.A.; Almer, J.; Misra, A. In situ X-ray investigation of freestanding nanoscale Cu–Nb multilayers under tensile load. *Appl. Phys. Lett.* **2009**, *94*, 217. [[CrossRef](#)]
106. Valiev, R. Materials science: Nanomaterial advantage. *Nature* **2002**, *419*, 887–889. [[CrossRef](#)] [[PubMed](#)]
107. Bhattacharyya, D.; Mara, N.A.; Dickerson, P.; Hoagland, R.G.; Misra, A. Compressive flow behavior of Al–TiN multilayers at nanometer scale layer thickness. *Acta Mater.* **2011**, *59*, 3804–3816. [[CrossRef](#)]
108. Carpenter, J.S.; Vogel, S.C.; Ledonne, J.E.; Hammon, D.L.; Beyerlein, I.J.; Mara, N.A. Bulk texture evolution of Cu–Nb nanolamellar composites during accumulative roll bonding. *Acta Mater.* **2012**, *60*, 1576–1586. [[CrossRef](#)]
109. Anderson, P.M.; Bingert, J.F.; Misra, A.; Hirth, J.P. Rolling textures in nanoscale Cu/Nb multilayers. *Acta Mater.* **2003**, *51*, 6059–6075. [[CrossRef](#)]
110. Misra, A.; Kung, H.; Hammon, D.L.G.; Hoagland, R.G. Damage mechanisms in nanolayered metallic composites. *Int. J. Damage Mech.* **2003**, *12*, 365–376. [[CrossRef](#)]
111. Misra, A.; Hoagland, R.G. Plastic flow stability of metallic nanolaminate composites. *J. Mater. Sci.* **2007**, *42*, 1765–1771. [[CrossRef](#)]
112. Zhu, X.F.; Li, Y.P.; Zhang, G.P.; Tan, J.; Liu, Y. Understanding nanoscale damage at a crack tip of multilayered metallic composites. *Appl. Phys. Lett.* **2008**, *92*, 161. [[CrossRef](#)]
113. Hsia, K.J.; Suo, Z.; Yang, W. Cleavage due to dislocation confinement in layered materials. *J. Mech. Phys. Solids* **1993**, *42*, 877–896. [[CrossRef](#)]
114. Hertzberg, R.W. *Deformation and Fracture Mechanics of Engineering Materials*; John Wiley: New York, NY, USA, 1989.

115. Chen, I.W.; Winn, E.J.; Menon, M. Application of deformation instability to microstructural control in multilayer ceramic composites. *Mater. Sci. Eng. A* **2001**, *317*, 226–235. [[CrossRef](#)]
116. Pathak, S.; Velisavljevic, N.; Baldwin, J.K.; Jain, M.; Zheng, S.; Mara, N.A. Strong, ductile, and thermally stable bcc-Mg nanolaminates. *Sci. Rep.* **2017**, *7*, 8264. [[CrossRef](#)] [[PubMed](#)]
117. Leyland, A.; Matthews, A. Design criteria for wear-resistant nanostructured and glassy-metal coatings. *Surf. Coat. Technol.* **2004**, *177*, 317–324. [[CrossRef](#)]
118. Volinsky, A.A.; Moody, N.R.; Gerberich, W.W. Interfacial toughness measurements for thin films on substrates. *Acta Mater.* **2002**, *50*, 441–466. [[CrossRef](#)]
119. Gerberich, W.W.; Cordill, M.J. Physics of adhesion. *Rep. Prog. Phys.* **2006**, *69*, 2157. [[CrossRef](#)]
120. Letierrier, Y. Durability of nanosized oxygen-barrier coatings on polymers. *Prog. Mater. Sci.* **2003**, *48*, 1–55. [[CrossRef](#)]
121. Song, G.M.; Vystavel, T.; Pers, N.V.D.; Hosson, J.T.M.D.; Sloof, W.G. Relation between microstructure and adhesion of hot dip galvanized zinc coatings on dual phase steel. *Acta Mater.* **2012**, *60*, 2973–2981. [[CrossRef](#)]
122. Zhou, Q.; Ren, Y.; Du, Y.; Hua, D.P.; Han, W.C.; Xia, Q.S. Adhesion energy and related plastic deformation mechanism of Cu/Ru nanostructured multilayer film. *J. Alloy. Compd.* **2018**. [[CrossRef](#)]
123. Hutchinson, J.W.; Suo, Z. Mixed mode cracking in layered materials. *Adv. Appl. Mech.* **1992**, *29*, 63–191.
124. Zinkle, S.J.; Busby, J.T. Structural materials for fission & fusion energy. *Mater. Today* **2009**, *12*, 12–19.
125. Stoller, R.E.; Odette, G.R. Effect of helium on swelling in stainless steel: Influence of cavity density and morphology. *Am. Soc. Test. Mater. Spec. Tech. Publ.* **1982**, 782. [[CrossRef](#)]
126. Lucas, A.A. Helium in metals. *Phys. B C* **1984**, *127*, 225–239. [[CrossRef](#)]
127. Trinkaus, H.; Singh, B.N. Helium accumulation in metals during irradiation—Where do we stand? *J. Nucl. Mater.* **2003**, *323*, 229–242. [[CrossRef](#)]
128. Hattar, K.; Demkowicz, M.J.; Misra, A.; Robertson, I.M.; Hoagland, R.G. Arrest of He bubble growth in cu–nb multilayer nanocomposites. *Scr. Mater.* **2008**, *58*, 541–544. [[CrossRef](#)]
129. Wolfer, W.G. The role of gas pressure and lateral stress on blistering. *J. Nucl. Mater.* **1980**, *93*, 713–720. [[CrossRef](#)]
130. Han, W.Z.; Demkowicz, M.J.; Fu, E.G.; Wang, Y.Q.; Misra, A. Effect of grain boundary character on sink efficiency. *Scr. Mater.* **2012**, *60*, 6341–6351. [[CrossRef](#)]
131. Fu, E.G.; Misra, A.; Wang, H.; Shao, L.; Zhang, X. Interface enabled defects reduction in helium ion irradiated Cu/V nanolayers. *J. Nucl. Mater.* **2010**, *407*, 178–188. [[CrossRef](#)]
132. Zinkle, S.J.; Matsukawa, Y. Observation and analysis of defect cluster production and interactions with dislocations. *J. Nucl. Mater.* **2004**, *329*, 88–96. [[CrossRef](#)]
133. Kocks, U.F. The theory of an obstacle-controlled yield strength—Report after an international workshop. *Mater. Sci. Eng.* **1977**, *27*, 291–298. [[CrossRef](#)]
134. Friedel, J. *Dislocation*; Pergamon Press: Oxford, UK, 1964.
135. Fleischer, R.L. Solution hardening by tetragonal distortions: Application to irradiation hardening in f.c.c. crystals. *Acta Metall.* **1962**, *10*, 835–842. [[CrossRef](#)]
136. Yu, K.Y.; Sun, C.; Chen, Y.; Liu, Y.; Wang, H.; Kirk, M.A. Superior tolerance of Ag/Ni multilayers against Kr ion irradiation: An in situ study. *Philos. Mag.* **2013**, *93*, 3547–3562. [[CrossRef](#)]
137. Höchbauer, T.; Misra, A.; Hattar, K.; Hoagland, R.G. Influence of interfaces on the storage of ion-implanted He in multilayered metallic composites. *J. Appl. Phys.* **2005**, *98*, 20. [[CrossRef](#)]
138. Zhang, X.; Li, N.; Anderoglu, O.; Wang, H.; Swadener, J.G.; Höchbauer, T. Nanostructured Cu/Nb multilayers subjected to helium ion-irradiation. *Nucl. Inst. Methods Phys. Res. B* **2007**, *261*, 1129–1132. [[CrossRef](#)]
139. Demkowicz, M.J.; Bhattacharyya, D.; Usov, I.; Wang, Y.Q.; Nastasi, M.; Misra, A. The effect of excess atomic volume on He bubble formation at fcc–bcc interfaces. *Appl. Phys. Lett.* **2010**, *97*, 846. [[CrossRef](#)]
140. Demkowicz, M.J.; Misra, A.; Caro, A. The role of interface structure in controlling high helium concentrations. *Curr. Opin. Solid State Mat. Sci.* **2012**, *16*, 101–108. [[CrossRef](#)]
141. Sharma, G.; Sarkar, A.; Varshney, J.; Ramamurty, U.; Kumar, A.; Gupta, S.K. Effect of irradiation on the microstructure and mechanical behavior of nanocrystalline nickel. *Scr. Mater.* **2011**, *65*, 727–730. [[CrossRef](#)]
142. Tan, X.H.; Shen, Y.L. Modeling analysis of the indentation-derived yield properties of metallic multilayered composites. *Compos. Sci. Technol.* **2005**, *65*, 1639–1646. [[CrossRef](#)]
143. Zhang, G.P.; Liu, Y.; Wang, W.; Tan, J. Experimental evidence of plastic deformation instability in nanoscale Au/Cu multilayers. *Appl. Phys. Lett.* **2006**, *88*, 2025–2028. [[CrossRef](#)]

144. Li, Y.P.; Tan, J.; Zhang, G.P. Interface instability within shear bands in nanoscale Au/Cu multilayers. *Scr. Mater.* **2008**, *59*, 1226–1229. [[CrossRef](#)]
145. Xie, J.Y.; Huang, P.; Wang, F.; Li, Y.; Xu, K.W. Shear banding behavior in nanoscale Al/W multilayers. *Surf. Coat. Technol.* **2013**, *228*, S593–S596. [[CrossRef](#)]
146. Zhu, X.F. Two different types of shear-deformation behaviour in Au–Cu multilayers. *Philos. Mag. Lett.* **2009**, *89*, 66–74.
147. Dayal, P.; Quadir, M.Z.; Kong, C.; Savvides, N.; Hoffman, M. Transition from dislocation controlled plasticity to grain boundary mediated shear in nanolayered aluminum/palladium thin films. *Thin Solid Films* **2011**, *519*, 3213–3220. [[CrossRef](#)]
148. Clemens, B.M.; Nix, W.D.; Ramaswamy, V. Surface-energy-driven intermixing and its effect on the measurement of interface stress. *J. Appl. Phys.* **2000**, *87*, 2816–2820. [[CrossRef](#)]
149. Zhou, Q.; Li, S.; Huang, P.; Xu, K.W.; Wang, F.; Lu, T.J. Strengthening mechanism of super-hard nanoscale Cu/Al multilayers with negative enthalpy of mixing. *Appl. Mater.* **2016**, *4*, 012102. [[CrossRef](#)]
150. Wei, X.Z.; Zhou, Q.; Xu, K.W.; Huang, P.; Wang, F.; Lu, T.J. Enhanced hardness via interface alloying in nanoscale Cu/Al multilayers. *Mater. Sci. Eng. A* **2018**, 726. [[CrossRef](#)]
151. Kwon, K.W.; Lee, H.J.; Sinclair, R. Solid-state amorphization at tetragonal-Ta/Cu interfaces. *Appl. Phys. Lett.* **1999**, *75*, 935–937. [[CrossRef](#)]
152. Fan, Z.; Xue, S.; Wang, J.; Yu, K.Y.; Wang, H.; Zhang, X. Unusual size dependent strengthening mechanisms of Cu/amorphous CuNb multilayers. *Acta Mater.* **2016**, *120*, 327–336. [[CrossRef](#)]
153. Mckeown, J.; Misra, A.; Kung, H.; Hoagland, R.G.; Nastasi, M. Microstructures and strength of nanoscale Cu–Ag multilayers. *Scr. Mater.* **2002**, *46*, 593–598. [[CrossRef](#)]
154. Misra, A.; Kung, H.; Mitchell, T.E.; Nastasi, M. Residual stresses in polycrystalline Cu/Cr multilayered thin films. *J. Mater. Res.* **2000**, *15*, 756–763. [[CrossRef](#)]
155. Zheng, S.J.; Wang, J.; Carpenter, J.S.; Mook, W.M.; Dickerson, P.O.; Mara, N.A. Plastic instability mechanisms in bimetallic nanolayered composites. *Acta Mater.* **2014**, *79*, 282–291. [[CrossRef](#)]
156. Li, Y.P.; Zhu, X.F.; Tan, J.; Wu, B.; Wang, W.; Zhang, G.P. Comparative investigation of strength and plastic instability in Cu/Au and Cu/Cr multilayers by indentation. *J. Mater. Res.* **2009**, *24*, 728–735. [[CrossRef](#)]



© 2018 by the authors. Licensee MDPI, Basel, Switzerland. This article is an open access article distributed under the terms and conditions of the Creative Commons Attribution (CC BY) license (<http://creativecommons.org/licenses/by/4.0/>).